

# Primordial Black Holes as Dark Matter and the Tachyonic Trap During Inflation

Yuma S. Furuta

*School of High Energy Accelerator Science, Graduate University for Advanced Studies (SOKENDAI), 1-1 Oho, Tsukuba, Ibaraki 305-0801, Japan and*

*Theory Center, IPNS, High Energy Accelerator Research Organization (KEK), 1-1 Oho, Tsukuba, Ibaraki 305-0801, Japan*

Mindaugas Karčiauskas

*Center for Physical Sciences and Technology (FTMC), Saulėtekio av. 3, 10257 Vilnius, Lithuania*

Kazunori Kohri

*Division of Science, National Astronomical Observatory of Japan, 2-21-1 Osawa, Mitaka, Tokyo 181-8588, Japan*

*School of Physical Sciences, Graduate University for Advanced*

*Studies (SOKENDAI), 2-21-1 Osawa, Mitaka, Tokyo 181-8588, Japan*

*Theory Center, IPNS, High Energy Accelerator Research Organization (KEK), 1-1 Oho, Tsukuba, Ibaraki 305-0801, Japan and  
Kavli IPMU (WPI), UTIAS, The University of Tokyo, Kashiwa, Chiba 277-8583, Japan*

Alejandro Sáez

*Instituto de Física Corpuscular (IFIC), CSIC-Universitat de València, 46071, Valencia, Spain*

We show that resonant processes during multi-field inflation can generate a large curvature perturbation on small scales. This perturbation naturally leads to the formation of primordial black holes that may constitute dark matter, as well as to the production of stochastic induced gravitational waves in the deci-Hz band. Such waves are within reach of future space-based interferometers such as LISA, DECIGO and BBO. In addition, primordial black hole binaries formed at late times produce merger gravitational waves that can be probed by the resonant cavity experiments in addition to DECIGO and BBO.

## I. INTRODUCTION

In several multi-field inflationary scenarios, the Universe undergoes multiple-field transitions during inflation, analogous to phase transitions. Identifying the role of these transitions through observations could provide decisive information about the ultimate theory to describe the early Universe.

In some of these models, interactions between fields can cause resonant field excitations during inflation. A classical example is the so called “Trapped Inflation” [1, 2]. But resonances during inflation and their impact on the primordial perturbation had been studied even earlier, for example, in Ref. [3–5] (for some later works see Ref. [6–9]). Many of the works are based on the mechanism suggested in Ref. [1], where moduli fields of string theory are stabilised by the backreaction of resonantly produced particles. As moduli field(s) pass through or close to (in the case of multi-field inflation) a critical point in field space, some real scalar field  $\chi$  is rendered massless. Thus, this point was naturally denoted by the name “Enhanced Symmetry Point” (ESP) in Ref. [1]. Around ESP the effective mass of  $\chi$  is changing non-adiabatically, which induces resonant excitations. The excitations backreact onto the motion of the inflaton, modifying its dynamics.

In this work we consider a somewhat modified scenario. Instead of the field  $\chi$  becoming massless at the critical point, we allow it to become tachyonic, i.e. its mass squared to become negative. Hence, for some parameter values the resonance resembles the one studied in Ref. [10], which they called “Tachyonic Resonance”. To emphasise this difference, we name the critical point as the “Symmetry Breaking Point” (SBP). The idea for such a scenario is inspired by the tachyonic trap mechanism, employed to provide an alternative method of reheating for non-oscillatory potentials and to prevent the scalar field of the quintessential inflation scenario from reaching superplanckian values [11, 12].

The current scenario is explored in the context of the supersymmetry-inspired multi-field running-mass model [13]. Augmenting the running-mass-inflation (RMI) with the tachyonic trap mechanism provides a concrete scenario by which inflation can end in a form similar to hybrid inflation [14, 15]. The current treatment, however, differs from the usual considerations of hybrid inflation. First, we take the waterfall phase, i.e. the evolution in the  $\chi$  direction in field space, to last more than 10 e-folds, which requires a very flat potential. In such a setup, the tachyonic trap becomes essential to redirect the field evolution from the RMI direction into the waterfall one, at least for parameter ranges considered in this work.

The tachyonic resonance at SBP has another important effect: it generates a sharp peak in the spectrum of the primordial perturbation  $\mathcal{P}_\zeta$  at small scales. The amplitude of that peak can be enhanced by several orders of magnitude

relative to the slow-roll result. Combined with the large spectral running of RMI, the spectrum can reach as high values as  $\mathcal{P}_\zeta \sim 10^{-1.5}$  [13, 16–22].

Later, upon horizon reentry in the early Universe, the large curvature perturbation can trigger gravitational collapse, leading to the formation of the primordial black holes (PBHs). As argued in Ref. [23] (for reviews, see also Refs. [24–26]), PBHs with masses in the range  $10^{17}$  g [27] –  $10^{23}$  g [28, 29] can serve as dark matter candidates. This scenario can be constrained or confirmed by future gamma-ray observations and related astrophysical probes [23].

Second, the same perturbations generate stochastic induced gravitational waves (SIGWs) through nonlinear second-order effects [30–38]. These SIGWs, peaking in the deci-Hz band, provide promising targets for future gravitational-wave detectors such as LISA, DECIGO, and BBO. In the current analysis, we incorporate recent refinements accounting for the dissipation of small-scale fluctuations [39], yielding state-of-the-art predictions for the SIGW spectrum.

Third, PBHs formed in the early Universe can assemble into binaries through many-body gravitational interactions [40–42]. The mergers of these binaries also generate a stochastic background of gravitational waves. Remarkably, such merger signals may be detectable not only by DECIGO and BBO but also through resonant cavity experiments exploiting the inverse Gertsenshtein effect [43, 44], originally proposed in the context of axion searches.

The remainder of this paper is organized as follows. In Sec. II, we outline the general framework of trapped inflation. Sec. III applies it to the running-mass model in supersymmetry. Sec. IV describes the trapping mechanism in details, and Sec. V quantifies the trapping duration during the second stage of inflation. Sec. VI reviews the basics of primordial curvature perturbations, and Sec. VII derives the PBH mass function. Sec. VIII presents the calculation of induced gravitational waves, while Sec. IX addresses gravitational waves from PBH binary mergers. Sec. X summarizes our conclusions. Technical details are collected in three appendices: in Appendix A, Primordial perturbations in the flat gauge, in Appendix B, Stochastic induced GWs, and, in Appendix C, Binary PBH merger GWs. We use the units where  $c = \hbar = 1$ ,  $m_{\text{Pl}} = (8\pi G)^{-1/2}$  and  $G$  is the Newton’s gravitational constant.

## II. THE MODEL

We study a multi-field model of inflation. The basic setup is reminiscent of the hybrid inflation scenario [14, 15] with some essential modifications. First, we consider the potential in the direction of the inflaton  $\phi$  to be completely flat at tree level. The slope is generated by radiative corrections. Such models are known by the name "Running-Mass-Inflation" (RMI) [45–47]. At one loop level, the shape of the potential is given by

$$V(\phi) = V_c [1 + U(\phi)] \quad (1)$$

where  $V_c$  is constant and  $U(\phi)$  is defined by

$$U(\phi) \equiv -\frac{1}{2} \frac{\phi^2}{m_{\text{Pl}}^2} \left( B - \frac{A}{\left(1 + \alpha \ln \frac{\phi}{m_{\text{Pl}}}\right)^2} \right) \quad (2)$$

The shape of  $U(\phi)$  for several values of  $\alpha$ ,  $A$  and  $B$  parameters is shown in Fig. 1.

In analogy to hybrid inflation scenario we add an additional field  $\chi$ . The potential in the  $\chi$  direction is of the hilltop type [48]. The simplest form of such a potential can be written as

$$V(\chi) = -\frac{1}{2} m^2 \chi^2 + \lambda \chi^4. \quad (3)$$

The crucial piece for this scenario is the interaction part of the Lagrangian, which we take to be [11, 12]

$$V_{\text{int}}(\phi, \chi) = \frac{1}{2} g^2 \chi^2 (\phi - \phi_{\text{SBP}})^2. \quad (4)$$

$\phi_{\text{SBP}}$  denotes the critical value at which  $V_{\text{int}}$  vanishes. We choose to call this point a "Symmetry Breaking Point" and denote it by  $\phi_{\text{SBP}}$  in order to make the relation to the mechanism discussed in Ref. [12] more suggestive, but also to emphasise that our scenario somewhat deviates from the standard hybrid inflation scenario.

The main role of the  $\chi$  field in hybrid inflation scenarios is to terminate inflation. It is called the waterfall field. In our scenario the main function of  $\chi$  is to trap  $\phi$  at the  $\phi_{\text{SBP}}$  value. This is achieved by the backreaction of resonantly produced  $\chi$  particles [1, 12], hence we also sometimes call  $\chi$  as the "trapping field". Another difference, as compared to the traditional hybrid scenario, is that the "waterfall" phase in this scenario lasts many e-folds. This is needed to extend inflation sufficiently long after  $\phi = \phi_{\text{SBP}}$  is reached, so that the horizon and flatness problems of Hot Big Bang

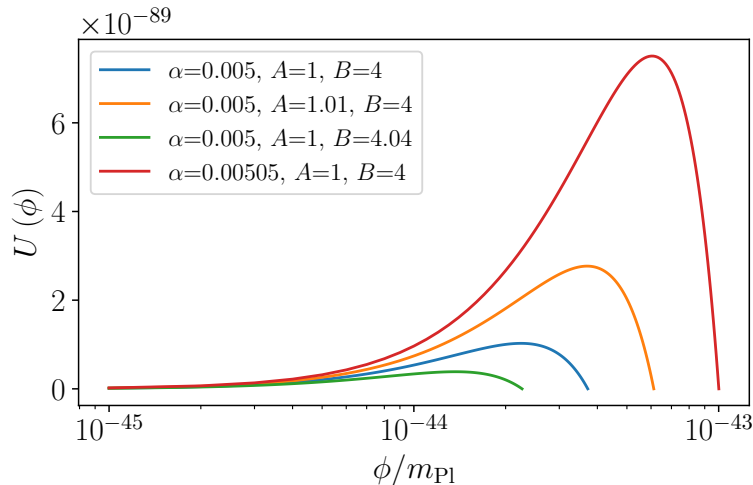


Figure 1. Rescaled RMI potential  $U(\phi)$  in Eq. (2) for several  $\alpha$ ,  $A$  and  $B$  values.

(HBB) are solved. Finally, as can be witnessed from Eq. (4), the  $\phi$ - $\chi$  interaction includes a trilinear term. Trilinear interactions can be found in the  $A$  term of SUGRA models [49], but it can also be generated by fermion condensation [50].

Adding all these components together, the full Lagrangian of the model can be written as

$$\mathcal{L} = -\frac{1}{2}(\partial_\mu\phi)^2 - V(\phi) - \frac{1}{2}(\partial_\mu\chi)^2 - V(\chi) - V_{\text{int}}(\phi, \chi) \quad (5)$$

The dynamics evolves over three stages. Initially the inflaton  $\phi$  is displaced far away from the critical value,  $\phi \gg \phi_{\text{SBP}}$ . This makes the trapping field  $\chi$  very heavy and anchored at the origin. During the first phase, while  $\phi$  rolls down towards the origin, the dynamics can be well approximated by slow-roll. Once  $\phi$  approaches  $\phi_{\text{SBP}}$  the second phase starts. The motion of  $\phi$  induces a non-adiabatic change in the effective mass of the trapping field via the interaction term in Eq. (4). This results in resonant excitations of  $\chi$ , which backreact onto the motion of  $\phi$  and anchors it at  $\phi_{\text{SBP}}$ . In the final phase, the  $\chi$  field rolls down the potential in Eq. (3), which is chosen to be sufficiently flat, so that inflation lasts for an additional  $\sim 10$  e-folds in this phase. Below we discuss these phases in more detail.

### III. RUNNING-MASS-INFLATION

Let  $\phi_*$  be the inflaton field value when the pivot scale exits the horizon during inflation. CMB observations allow us to constrain the primordial spectrum roughly 10 e-folds around this value. The first task is to find regions in  $(\alpha, A, B)$  parameter space where the model generates the primordial perturbation that is consistent with CMB observations.

Generically we take  $\phi_{\text{SBP}} \ll \phi_*$ , which, according to Eq. (4), makes the  $\chi$  field heavy and anchored at the origin, leading to an effectively single field inflation, at least within the 10 e-folds mentioned above. Another important consequence of  $\chi$  being heavy is that the isocurvature perturbation is suppressed at CMB scales, which makes the observational bounds on this parameter [51] easily satisfied.

One of the features of the RMI potential in Eq. (1) is that it becomes ever flatter as  $\phi$  field approaches the origin. This makes the inflaton dynamics eventually dominated by the kinetic energy rather than by the slope of the potential. In other words, inflation enters the ultra-slow-roll regime [52–55] if not terminated earlier. To investigate this issue we solved the homogeneous equations of motion numerically. One such solution is shown in Fig. 2.

As can be seen from Fig. 2, at larger inflaton values slow-roll provides a good description of the dynamics. During this period the inflaton equation of motion can be approximated by

$$\dot{\phi} \simeq -\frac{V_{,\phi}}{3H}, \quad (6)$$

where  $V$  is given in Eq. (1) and the index denotes the derivative with respect to the field  $\phi$ . In this approximation the Hubble parameter is dominated by the potential energy

$$3m_{\text{Pl}}^2 H^2 \simeq V(\phi) \simeq V_c, \quad (7)$$

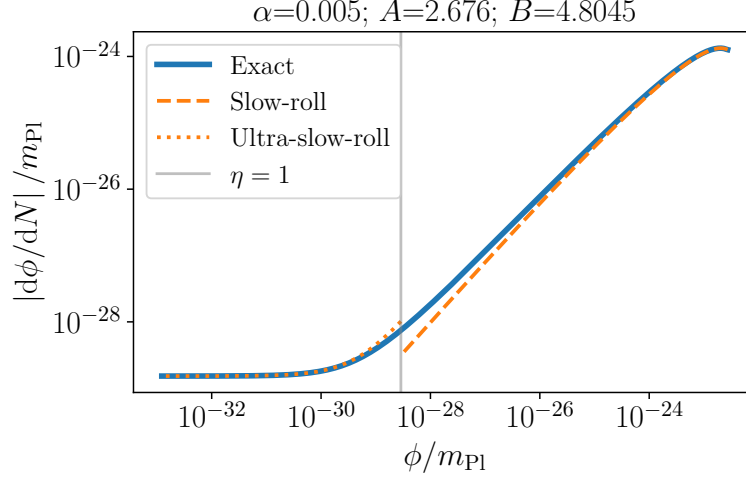


Figure 2. The numerical solution of homogeneous RMI equations (“Exact”). At the pivot scale, on the RHS of the plot, inflation is well approximated by slow-roll (cf. Eq. (6)), but eventually it enters the ultra-slow-roll regime (cf. Eq. (9)). Conventionally this transition is taken at  $\eta = 1$  (vertical gray line).

where  $V_c$  is defined in Eq. (1). This slow-roll approximated solution is denoted by the dashed curve in Fig. 2.

As  $\phi$  decreases, eventually inflation enters the ultra-slow-roll regime. In this regime the slope of the potential can be neglected, and we obtain an approximate equation of motion of the form

$$\ddot{\phi} \simeq -3H\dot{\phi}, \quad (8)$$

where  $H \simeq \text{const.}$  and its value can be computed using the same approximate expression in Eq. (7). It is easy to show that the approximate solution of the above equation is

$$\dot{\phi} \simeq \dot{\phi}_0 - 3H(\phi - \phi_0). \quad (9)$$

The ultra-slow-roll approximated solution is represented by the dotted curve in Fig. 2.

The approximate location in the potential, where slow-roll gives way to ultra-slow-roll, is conventionally taken to be  $\eta = 1$ , where  $\eta$  is the second slow-roll parameter defined bellow in Eq. (11).

To choose viable models, which do not contradict CMB constraints, we calculate the properties of the scalar perturbation spectrum and the amplitude of the tensor mode. Because slow-roll approximates the inflaton dynamics sufficiently well when CMB scales exit the horizon, we use the well known relations between the slow-roll parameters and the shape of the primordial spectrum. These parameters are defined in terms of the potential  $V(\phi)$  and its derivatives as

$$\epsilon = \frac{m_{\text{Pl}}^2}{2} \left( \frac{U_{,\phi}}{U+1} \right)^2, \quad (10)$$

$$\eta = m_{\text{Pl}}^2 \frac{U_{,\phi\phi}}{U+1}, \quad (11)$$

$$\xi^2 = m_{\text{Pl}}^4 \frac{U_{,\phi} U_{,\phi\phi\phi}}{(U+1)^2}, \quad (12)$$

$$\omega^3 = m_{\text{Pl}}^6 \frac{U_{,\phi}^2 U_{,\phi\phi\phi\phi}}{(U+1)^3}, \quad (13)$$

where  $U(\phi)$  is given in Eq. (2) and the indices denote derivatives with respect to the inflaton  $\phi$ . The spectral properties of the primordial scalar perturbation are related to the above parameters by the following expressions (see

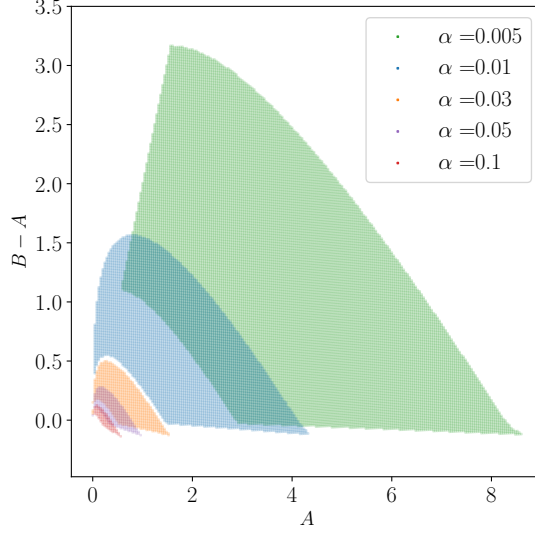


Figure 3. Parameter regions for several different  $\alpha$  values where the running mass inflation models are compatible with the CMB constraints on the primordial spectrum at the pivot scale  $k_* = 0.05 \text{ Mpc}^{-1}$  (Eqs. (18)–(21)). We also impose two other conditions:  $\phi_* < m_{\text{Pl}}$  when the pivot scale exits the horizon and that the energy scale of inflation is larger than the Big Bang Nucleosynthesis (BBN) scale.

e.g. Ref. [48] or [56])

$$n_s \equiv \frac{d \ln A_s}{d \ln k} = 1 - 6\epsilon + 2\eta, \quad (14)$$

$$\alpha_s \equiv \frac{d \ln n_s}{d \ln k} = 16\epsilon\eta - 24\epsilon^2 - 2\xi^2, \quad (15)$$

$$\beta_s \equiv \frac{d^2 \ln n_s}{d \ln k^2} = -192\epsilon^3 + 192\epsilon^2\eta - 32\epsilon\eta^2 - 24\epsilon\xi^2 + 2\eta\xi^2 + 2\omega^3, \quad (16)$$

where  $n_s$ ,  $\alpha_s$  and  $\beta_s$  are the scalar spectral index, its running and the running-of-the-running respectively. All of these quantities are to be computed when the pivot scale exits the horizon. Analogously, tensor-to-scalar ratio can also be related to the slow-roll parameter  $\epsilon$  by

$$r = 16\epsilon. \quad (17)$$

To find models that are compatible with observations we scan over the parameters  $\alpha$ ,  $A$  and  $B$  and look for regions of  $\phi_*$  values that result in the primordial spectrum with values in the range

$$n_s = 0.9743 \pm 0.0034, \quad (18)$$

$$\alpha_s = 0.0062 \pm 0.0052, \quad (19)$$

$$\beta_s = 0.010 \pm 0.013. \quad (20)$$

The errorbars correspond to  $1\sigma$  constraints for  $n_s$  [57],  $\alpha_s$  [58] and  $\beta_s$  [51]. To constrain the tensor-to-scalar ratio we adopt the upper bound in Ref. [59]

$$r < 0.036. \quad (21)$$

The final PBH abundance is not very sensitive to the precise values of these parameters. They only determine which model in the  $(\alpha, A, B)$  plane will be used to represent the inflaton direction. The result of the scan over this parameter space is shown in Fig. 3 for several values of  $\alpha$ .

Usually all the constraints in Eqs. (18)–(21) can be satisfied only for a small range of  $\phi$  values, if at all. For such models we choose  $\phi_*$  to correspond to the value that is closest to the central value of the constraints. Once  $\phi_*$  is fixed, we can compute the energy scale of inflation  $V_c$  from the amplitude of the scalar spectral index  $A_s$ , given by

$$A_s = \frac{V}{24m_{\text{Pl}}^2\epsilon}. \quad (22)$$

The value of  $A_s$  is fixed by the Planck normalisation,  $A_s = 3.044$  [51].

Initially  $\phi$  follows the slow-roll equation of motion in Eq. (6). As the potential flattens out the dynamics becomes well approximated by ultra-slow-roll in Eq. (9). The latter equation is solved by

$$\dot{\phi} \propto a^{-3}. \quad (23)$$

One of the consequences of the flattening of the potential is the rapid increase in the amplitude of the curvature perturbation  $\mathcal{P}_\zeta$ . On superhorizon scales it can be written as

$$\mathcal{P}_\zeta(k) = \left(\frac{H}{\dot{\phi}}\right)^2 |\delta\phi_k|^2, \quad (24)$$

where  $\delta\phi_k(t)$  is the Fourier mode of the field perturbation  $\delta\phi(x, t)$ . We can see that as  $\dot{\phi}$  decreases,  $\mathcal{P}_\zeta$  rapidly grows. We must make sure that the first phase of inflation is terminated before  $\mathcal{P}_\zeta$  reaches the value of 1. Otherwise perturbations become non-linear, which is in conflict with observations [60, 61].

#### IV. THE TRAPPING PHASE

To the best of our knowledge there is no detailed discussion in the literature of a mechanism to end the RMI phase and provide the remaining e-folds of inflation. Usually it is implicitly assumed that hybrid inflation or some related mechanism terminates the RMI stage before  $\mathcal{P}_\zeta(k)$  becomes too large. Unfortunately, a simplistic implementation of hybrid inflation is difficult to realise. After observable scales – where  $\mathcal{P}_\zeta(k_*)$  is fixed to satisfy CMB bounds – exit the horizon, the maximum value of  $\mathcal{P}_\zeta(k)$  must be reached in about 30-35 e-folds. Only then the masses of PBHs created by a large curvature perturbation are such that they can explain the observed DM abundance (see Fig. 7). But 30-35 fall short from the expected 50-60 e-folds of inflation, which are required to solve the flatness and horizon problems of HBB (see section V for a more detailed discussion). Therefore, to solve these problems inflation must last for an additional  $\sim 10$  e-folds in the waterfall phase. A long waterfall phase can be achieved if the potential in this direction is flat enough. But we found that for a too flat potential the  $\phi$  field just zips through the critical (Symmetry Breaking) point without destabilising the waterfall field  $\chi$ .

Fortunately, as we show, this problem can be circumvented by another effect. For some parameter values the passage of  $\phi$  through the Symmetry Breaking Point  $\phi_{\text{SBP}}$  induces resonant excitations of the  $\chi$  field. This field backreacts onto the motion of  $\phi$  by making it effectively heavy and stopping it from rolling down the potential. This is the basic scenario of the tachyonic trap mechanism discussed in Refs. [11, 12]. In this work we make use of the tachyonic trap mechanism to terminate RMI at the value of  $\mathcal{P}_\zeta$  that results in the production of PBHs with masses that can explain Dark Matter [23]. A schematic depiction of our scenario is provided in Fig. 4.

##### A. The Tachyonic Trap

In Refs. [11, 12], where the tachyonic trapping mechanism is analysed, the metric perturbations are ignored. These simplifications can no longer be employed for the current model, where such perturbations play the central role. Nevertheless, before discussing the model in full detail, including the metric perturbation, below we summarize the basic ideas behind the tachyonic trap mechanism.

For the most part of the RMI stage of inflation the trapping field  $\chi$  is very heavy. This is the case if the value of the coupling constant  $g$  in Eq. (4) is not too small, so that  $g^2(\phi - \phi_{\text{SBP}})^2 \gg H^2$ , where  $H$  is the Hubble parameter during inflation. This makes the homogeneous component of the  $\chi$  field anchored at the origin. The perturbations  $\delta\chi$  of the  $\chi$  field obey the following equation of motion:

$$\delta\ddot{\chi}_k + 3H\delta\dot{\chi}_k + (\omega_k^2 + 12\lambda\langle\chi^2\rangle)\delta\chi_k \simeq 0, \quad (25)$$

where

$$\omega_k^2 \equiv \frac{k^2}{a^2} - m^2 + g^2(\phi - \phi_{\text{SBP}})^2 \quad (26)$$

We can rewrite the above equation in the canonical form by defining

$$X_k \equiv a\chi_k \quad (27)$$

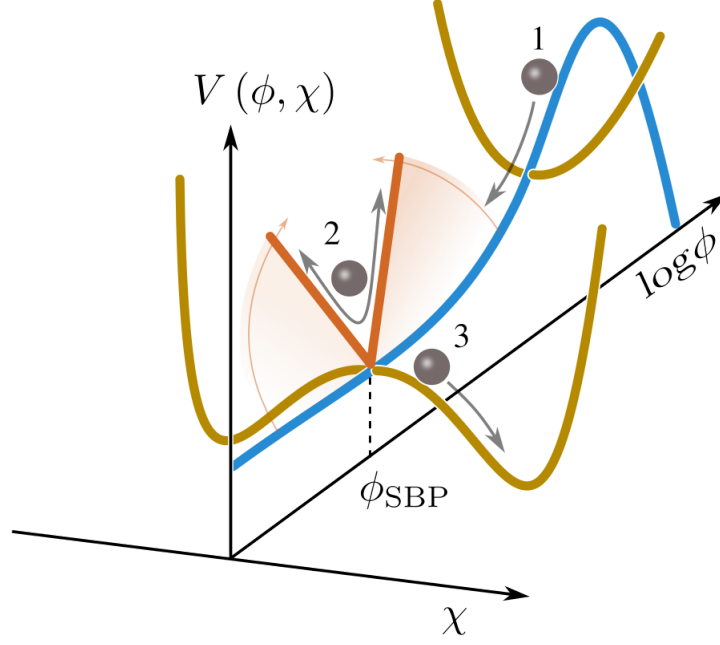


Figure 4. Schematic depiction of our scenario. At stage 1 the field rolls down along the RMI direction (blue curve). At tree level, the linear potential (red curve) does not exist. Once the field reaches SBP (stage 2) it resonantly excites the  $\chi$  field. Excitations backreact onto the motion of the field, which can be effectively described by a steepening linear potential. At this stage the trapped  $\phi$  field oscillates around  $\phi_{\text{SBP}}$  with an exponentially decreasing amplitude. Eventually the amplitude becomes too small to excite the  $\chi$  field. At that point the evolution enters the 3rd stage, in which the field rolls down solely in the direction of the sufficiently flat waterfall potential (brown curve) with  $\phi$  remaining being fixed at  $\phi_{\text{SBP}}$ . During stage 2 the metric perturbation is also resonantly amplified for scales which exit the horizon at that time.

and using the conformal time  $d\tau \equiv dt/a$ . This gives

$$X_k'' + (W_k^2 + 12\lambda a^2 \langle \chi^2 \rangle) X_k = 0, \quad (28)$$

where primes denote derivatives with respect to  $\tau$  and

$$W_k^2 \equiv a^2 \omega_k^2 - \frac{a''}{a}. \quad (29)$$

Initially, as field  $\phi$  is far away from SBP, the effective mass of the trapping field satisfies

$$m_{\text{eff}}^2 \equiv g^2 (\phi - \phi_{\text{SBP}})^2 - m^2 \simeq g^2 (\phi - \phi_{\text{SBP}})^2 \gg 12\lambda \langle \chi^2 \rangle \quad (30)$$

and Eq. (28) reduces to the equation of a harmonic oscillator with an adiabatically changing mass. We can thus impose the adiabatic vacuum initial conditions, which, at the lowest order, are given by

$$X_{k,\text{vac}}(\eta) = \frac{1}{\sqrt{2W_k}} e^{-i \int W_k d\eta}. \quad (31)$$

Up to the same order, the occupation number can be computed using the expression

$$n_k = \frac{W_k}{2} \left[ \frac{|X_k'|^2}{W_k^2} + |X_k|^2 \right] - \frac{1}{2}. \quad (32)$$

The  $12\lambda a^2 \langle \chi^2 \rangle$  term consists of the Hartree approximation to account for self-interactions, where the expectation value  $\langle \chi^2 \rangle$  can be computed using the equation

$$\langle \chi^2 \rangle = a^{-2} \langle X^2 \rangle = \frac{a^{-2}}{2\pi^2} \int dk k^2 \left[ |X_k|^2 - \frac{1}{2|W_k|} \right]. \quad (33)$$

As the  $\phi$  field moves towards the origin and comes close to  $\phi_{\text{SBP}}$  the effective mass squared  $m_{\text{eff}}^2$  vanishes and then becomes negative. Moreover, within some interval of  $\phi$  values the change of  $m_{\text{eff}}^2$  is rendered to be non-adiabatic [11, 12]. This causes two effects. First, the non-adiabaticity of  $m_{\text{eff}}^2$  results in the resonant excitations of the  $\chi$  field, as described in Ref. [62]. Second, as  $m_{\text{eff}}^2$  becomes negative, it can lead to an additional amplification of  $\chi$  field perturbations via the process known as the tachyonic resonance [10, 63].

Which of the two effects dominates, depends on model parameters [12]. But in both cases, due to  $\phi$ - $\chi$  interactions, the exponential growth of  $\langle \chi^2 \rangle$  backreacts onto the motion of the  $\phi$  field by creating an effective contribution to its mass term. Indeed, from Eq. (4) we find the effective equation of motion of the homogeneous component of the  $\phi$  field to be

$$\ddot{\phi} + 3H\dot{\phi} + V(\phi, \chi)_{,\phi} = 0, \quad (34)$$

where

$$V(\phi, \chi)_{,\phi} \simeq V_c U_{,\phi} + g^2 \langle \chi^2 \rangle (\phi - \phi_{\text{SBP}}) \quad (35)$$

and  $V_c$  and  $U$  are defined in Eqs. (1) and (2) respectively. Once the second term in the above expression becomes large enough,  $g^2 \langle \chi^2 \rangle > H^2$ , the field becomes heavy and stops running towards the origin, but rather oscillates around  $\phi_{\text{SBP}}$  with a decaying amplitude.

This process is somewhat similar to the one described in Ref. [1], where the resonant excitations of the  $\chi$  field traps the  $\phi$  field at SBP. In contrast to that work, we take  $\chi$  to be tachyonic. This way the trapping of  $\phi$  at  $\phi_{\text{SBP}}$  initiates the symmetry breaking phase by releasing the  $\chi$  field from the origin and allowing it to roll towards the vacuum value. This gives the name for the subscript  $\phi_{\text{SBP}}$ , as in ‘‘Symmetry Breaking Point’’ and the name ‘‘tachyonic trap’’ for the mechanism [12].

There is another crucial difference in the current model as compared to both Ref. [1] and [12]. The resonance and the trapping in the latter references are assumed to happen in a non-accelerating spacetime. In the current application, we make use of the tachyonic trap during inflation. The idea of resonant field excitations during inflation is not new. We can find such discussions in, for example, Refs. [3, 8, 64, 65] and many others. But here again, in contrast to those works, we consider  $\chi$  to be tachyonic. This allows for the  $\chi$  field to play the role of the waterfall field à la hybrid inflation.

## B. The Metric Perturbation

As it is well known in the literature of preheating, see e.g. Refs. [3, 8, 66–69], resonant processes also affect the metric perturbation. The current model is not an exception. In order to estimate these effects and to compute the final spectrum of the primordial curvature perturbation we employ semi-analytic computations. To that goal several simplifications are made. First of all, we will only solve linearised equations. It is likely that such an approximation provide sufficiently accurate results. In contrast to the preheating scenarios, perturbations during inflation must remain linear. This also justifies using the Hartree approximation to estimate the effects of non-linear terms. Due to the smallness of perturbations, we would expect non-linear  $k$ -mode interactions of the metric perturbation to not change the picture significantly.

At the linear level, we perform the computations in the Newtonian and flat gauges. The two gauges are used in order to check the consistency of our numerical code. We present Newtonian gauge equations in this section and analogous expressions in the flat gauge in Appendix A. The line element in the former takes the form

$$ds^2 = -(1 + 2\Phi) dt^2 + a^2(t) (1 + 2\Psi) \delta_{ij} dx^i dx^j. \quad (36)$$

Since this is a two scalar field model in General Relativity, the anisotropic stress vanishes and the two metric perturbation variables are related by  $\Psi = -\Phi$ . Therefore we can drop  $\Psi$  in favour of  $\Phi$ .

Scalar fields  $\phi$  and  $\chi$  are also perturbed such that

$$\phi(\mathbf{x}, t) = \bar{\phi}(t) + \delta\phi(\mathbf{x}, t) \quad (37)$$

and

$$\chi(\mathbf{x}, t) = \bar{\chi}(t) + \delta\chi(\mathbf{x}, t). \quad (38)$$

In the case of the  $\phi$  field we have  $\bar{\phi} \gg \delta\phi$ , therefore the separation into the homogeneous value  $\bar{\phi}$  and the perturbation  $\delta\phi$  is unambiguous. In regards to the  $\chi$  field, an analogous separation is more subtle. Initially  $\chi$  is heavy and its VEV vanishes. Hence, we define  $\bar{\chi}$  by

$$\bar{\chi} \equiv \sqrt{\langle \chi^2 \rangle}, \quad (39)$$



where  $\langle \chi^2 \rangle$  is given in Eq. (33) and we take  $\delta\chi$  to be of the same perturbation order as  $\delta\phi$ . Finally, because we have no use of the full fields  $\phi(\mathbf{x}, t)$  and  $\chi(\mathbf{x}, t)$ , we will drop the overbars from the homogeneous fields and denote them just by  $\phi$  and  $\chi$  in the remaining part of the text.

The homogeneous components follow the equations

$$\ddot{\phi} + 3H\dot{\phi} + V_{,\phi} = 0, \quad (40)$$

$$\ddot{\chi} + 3H\dot{\chi} + V_{,\chi} = 0, \quad (41)$$

where the Hubble parameter is given by

$$3H^2 = \frac{1}{2}\dot{\phi}^2 + \frac{1}{2}\dot{\chi}^2 + V \quad (42)$$

and  $V$  denotes the full potential

$$V \equiv V(\phi) + V(\chi) + V_{\text{int}}(\phi, \chi). \quad (43)$$

In regards to perturbations, the full system of equations in the Newtonian gauge is given by

$$\delta\ddot{\phi}_k + 3H\delta\dot{\phi}_k + \left(\frac{k^2}{a^2} + V_{,\phi\phi}\right)\delta\phi_k = 2\left(2\dot{\phi}\dot{\Phi}_k - V_{,\phi}\Phi_k\right) - V_{,\phi\chi}\delta\chi_k, \quad (44)$$

$$\delta\ddot{\chi}_k + 3H\delta\dot{\chi}_k + \left(\frac{k^2}{a^2} + V_{,\chi\chi}\right)\delta\chi_k = 2\left(2\dot{\chi}\dot{\Phi}_k - V_{,\chi}\Phi_k\right) - V_{,\phi\chi}\delta\phi_k, \quad (45)$$

$$\dot{\Phi}_k + H\Phi_k = \frac{1}{2}\left(\dot{\phi}\delta\phi_k + \dot{\chi}\delta\chi_k\right), \quad (46)$$

where  $\delta\phi_k$ ,  $\delta\chi_k$  and  $\Phi_k$  represent the Fourier modes of perturbation variables  $\delta\phi$ ,  $\delta\chi$  and  $\Phi$  respectively. We use Eq. (46) in the integral form to inspect numerical solutions. In this form the equation can be written as

$$\Phi_k = \frac{1}{2a} \int a \left( \dot{\phi}\delta\phi_k + \dot{\chi}\delta\chi_k \right) dt. \quad (47)$$

In addition, the perturbed Einstein equation results in a constraint equation

$$\left(\dot{\phi}^2 + \dot{\chi}^2 - 2\frac{k^2}{a^2}\right)\Phi_k = \dot{\phi}\delta\dot{\phi}_k + \dot{\chi}\delta\dot{\chi}_k - \ddot{\phi}\delta\phi_k - \ddot{\chi}\delta\chi_k. \quad (48)$$

Similarly to Eq. (25), using the Hartree approximation we replace  $\chi^2$  with  $\langle \chi^2 \rangle$  whenever such a term appears in Eqs. (44)–(46). For example,

$$V_{,\chi\chi} = g^2(\phi - \phi_{\text{SBP}})^2 - m^2 + 12\lambda\langle \chi^2 \rangle. \quad (49)$$

Eq. (46) makes it clear that  $\Phi_k$  is directly sourced by the trapping field perturbation  $\delta\chi_k$ . Hence, if  $\delta\chi_k$  is resonantly amplified, one expects that it also amplifies the metric perturbation. As we will see below, this is exactly what happens during the resonance.

The ultimate goal of solving these equations is to compute the primordial curvature perturbation  $\zeta$ . In terms of the Newtonian metric perturbation it is given by

$$\zeta_k = \Phi_k + 2H \frac{\dot{\Phi}_k + H\Phi_k \left(1 + \frac{1}{3}\frac{k^2}{a^2 H^2}\right)}{\dot{\phi}^2 + \dot{\chi}^2}. \quad (50)$$

The power spectrum of  $\zeta_k$  is then computed using

$$\mathcal{P}_\zeta(k) = \frac{k^3}{2\pi^2} |\zeta_k|^2. \quad (51)$$

Since we consider the two field model, inevitably the isocurvature perturbation is also generated at some level. Such a perturbation can be computed using the following expression [70]

$$\mathcal{S}_k = \frac{2}{3} \frac{\delta V \left[ 3H \left( \dot{\phi}^2 + \dot{\chi}^2 \right) + \dot{V} \right] + \left[ \dot{\phi}\delta\dot{\phi}_k + \dot{\chi}\delta\dot{\chi}_k - \Phi_k \left( \dot{\phi}^2 + \dot{\chi}^2 \right) \right] \dot{V}}{\left( \dot{\phi}^2 + \dot{\chi}^2 \right) \left[ 3H \left( \dot{\phi}^2 + \dot{\chi}^2 \right) + 2\dot{V} \right]}, \quad (52)$$

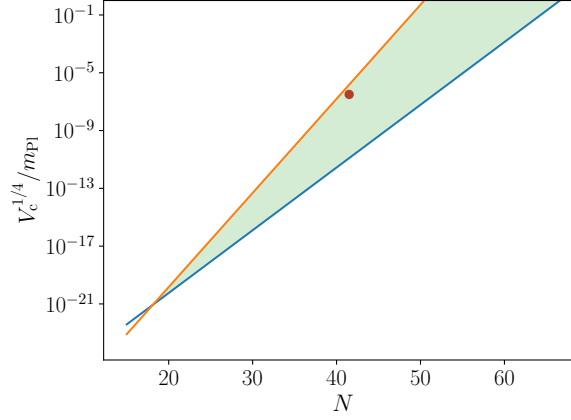


Figure 5. The allowed range of the energy scale of inflation (green shaded region). Orange and blue lines represent bounds in Eqs. (56) and (58) respectively. The red dot marks the value of the model specified in section VI.

where  $\delta V = V_{,\phi}\delta\phi + V_{,\chi}\delta\chi$ . Similarly to Eq. (51) we define the spectrum of the isocurvature perturbation to be

$$\mathcal{P}_S(k) = \frac{k^3}{2\pi^2} |\mathcal{S}_k|^2. \quad (53)$$

Because the  $\chi$  field is heavy when the pivot scale exits the horizon,  $\mathcal{S}_k$  is negligible on those scales (see Fig. 6 for an example). On smaller length scales, for modes exiting the horizon during the trapping phase, this is no longer true. As it is well known (see for example Ref. [70]) a non-zero isocurvature perturbation can source the curvature one, even on superhorizon scales. But this depends on the reheating scenario and other factors. Since we assume prompt reheating for the purpose of this work, we do not include the contribution from  $\mathcal{S}_k$  to  $\zeta_k$  during the post inflationary evolution. The study of these effects and their consequences for the mass distribution of PBHs is left for future work.

Furthermore, as pointed out in [71], the stochastic effect may become dominant in hybrid inflation with a waterfall under certain conditions. Therefore, we compare the classical effects,  $m_{\text{Pl}}^2 V_{,\phi}/V$  and  $m_{\text{Pl}}^2 V_{,\chi}/V$ , in the Friedmann equations with the quantum effect,  $H/2\pi$  [72]. We calculated the ratios defined as  $\Delta_\phi \equiv HV/2\pi m_{\text{Pl}}^2 V_{,\phi}$  and  $\Delta_\chi \equiv HV/2\pi m_{\text{Pl}}^2 V_{,\chi}$ . In the case of our hybrid inflation potential, both  $\Delta_\phi \sim 10^{-10}$  and  $\Delta_\chi \sim 10^{-15}$  were found to be small, indicating that the stochastic effect is negligible and a classical treatment is justified.

## V. THE SECOND STAGE AND THE TOTAL DURATION OF INFLATION

One of the traditional issues related to RMI is its large spectral running [17, 22]. Usually it takes only a few tens of e-folds of inflation before perturbations become non-linear. Such a short inflation is not sufficient if it is to solve the horizon and flatness problems. The duration of inflation can be enlarged if the  $V(\chi)$  part of the potential is flat enough, so that the waterfall phase can provide the missing number of e-folds. This is in contrast to the standard picture of hybrid inflation [14, 15], where the waterfall phase is assumed to be completed within less than an e-fold.

For this purpose we consider a hilltop type potential in Eq. (3), which consists of two free parameters  $m$  and  $\lambda$ . Only these two terms are assumed to be significant during the waterfall. Higher order terms can be added to stabilise the potential, but they are taken to be inconsequential for the dynamics of inflation.

To estimate the minimum number of e-folds of inflation that is required to solve the flatness and horizon problems of HBB we assume prompt reheating at the end of inflation. In this approximation we can write [48]

$$N \simeq 56 - \frac{2}{3} \ln \frac{10^{16} \text{ GeV}}{\rho_*^{1/4}} - \frac{1}{3} \ln \frac{10^9 \text{ GeV}}{T_{\text{reh}}}, \quad (54)$$

where  $N$  is the number of e-folds defined by  $N \equiv \ln a/a_0$ ,  $\rho_*^{1/4}$  is the energy scale of inflation when the pivot scale leaves the horizon in units of GeV and  $T_{\text{reh}}$  is the temperature at reheating, also in GeV. We can invert this expression and write

$$\frac{T_{\text{reh}}}{\text{MeV}} \simeq 1.7 \times 10^7 e^{3(N-56)} \frac{m_{\text{Pl}}^2}{\sqrt{V_c}}, \quad (55)$$

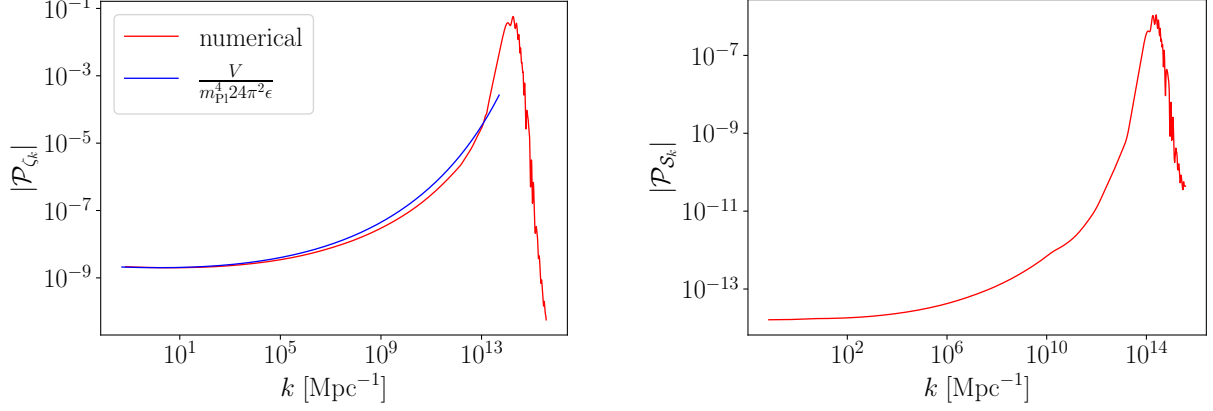


Figure 6. Left panel: the primordial curvature perturbation spectrum  $\mathcal{P}_\zeta(k)$  (see Eq. (51)). The red curve indicates numerical results. For comparison we also show (the blue curve) the spectrum computed using the slow-roll approximation (see Eq. (60)). This curve terminates at the scales that exit the horizon when  $\phi = \phi_{\text{SBP}}$ . Right panel: the spectrum of the isocurvature perturbation  $\mathcal{P}_S(k)$  (see Eq. (53))

where  $V_c$  is defined in Eq. (1) and we used the fact that  $U(\phi) \ll 1$ . There are (at least) two conditions that this equation must satisfy. First, the reheating temperature must be larger than the temperature of the Big Bang Nucleosynthesis, which is  $T_{\text{BBN}} \sim 1$  MeV [73–75]. It follows from the above equation that the upper bound on the energy scale of inflation must be

$$V_c < 3 \times 10^{14} \cdot e^{6(N-56)} m_{\text{Pl}}^4. \quad (56)$$

On the other hand, for a given duration and the energy scale of inflation, one must make sure that blindly applying Eq. (55) does not lead to the energy density  $\rho_{\text{reh}}$  at reheating to become larger than the energy scale at the end of inflation. For this estimate it will be sufficient to assume constant energy density during inflation and use the relation of the thermalised radiation

$$\rho_{\text{reh}} = \frac{\pi^2 g_*}{30} T_{\text{reh}}^4, \quad (57)$$

where  $g_*$  is the effective number of relativistic degrees of freedom. At temperatures  $T > 100$  GeV this number is  $g_* = \mathcal{O}(100)$ . Thus, we find from Eq. (55) that the condition  $V_{\text{end}} > \rho_{\text{reh}}$ , where  $V_{\text{end}}$  is the energy scale at the end of inflation, leads to the inequality

$$V_c > 10^{-19} \left( \frac{\pi^2 g_*}{30} \right)^{\frac{1}{3}} e^{4(N-56)} m_{\text{Pl}}^4, \quad (58)$$

where we took  $(V_c/V_{\text{end}})^{\frac{1}{3}} \sim 1$ .

Putting Eqs. (56) and (58) together and taking  $g_* = 150$  for concreteness and a rough estimate, we find

$$5 \times 10^{-19} e^{4(N-56)} < \frac{V_c}{m_{\text{Pl}}^4} < 3 \times 10^{14} \cdot e^{6(N-56)}. \quad (59)$$

This bound is easier to appreciate looking at Fig. 5. When searching for a viable parameter space of this model, the above condition, together with Eqs. (18)–(21), needs to be satisfied.

The effects of radiative corrections to the dynamics of the waterfall field [76] are ignored in this study. We don't expect such corrections to change the picture qualitatively. But their effect on the space of allowed parameter values should certainly be studied, which we plan to do in the future.

## VI. THE PRIMORDIAL CURVATURE PERTURBATION

To find models that are compatible with observations and provide large enough primordial perturbation on small scales, we perform numerical simulations. To do that, we first estimate the spectrum using slow-roll approximation

for all models in the allowed regions shown in Fig. 3. This narrows down the set of models which are likely to produce the correct amplitude of the spectrum at the required scales.

We next perform numerical simulations of the exact linear equations Eqs. (40)–(46) applied to this narrowed down set of models. Our goal is to find models that give the spectrum with a sharp peak of amplitude  $\mathcal{P}_\zeta(k_{\text{max}}) \simeq 10^{-1.5}$  at around 35 e-folds after the pivot scale exits the horizon. Such values are likely to lead to the correct mass distribution of PBHs, as discussed in sec. VII.

The parameters of one such model, which we continue using for the rest of the paper, are  $\alpha = 0.005$ ,  $A = 4.849$ ,  $B = 5.859$ . We found that for this model CMB constraints in Eqs. (18)–(21) are best satisfied when the inflaton field value is  $\phi_* = 3.89 \times 10^{-9} m_{\text{Pl}}$ . Consequently, this leads to the energy scale of inflation  $V_c^{1/4} = 10^{-6.5} m_{\text{Pl}}$ .  $N = 35$  e-folds later the inflaton reaches  $\phi_{\text{SBP}} = 6.02 \times 10^{-13} m_{\text{Pl}}$ . At this moment the trapping field is resonantly excited and rendered unstable. We ran a number of simulations to search for parameter values of the waterfall potential that give the right value of  $\mathcal{P}_\zeta$  and guarantee a long enough waterfall phase. One such possible model resulted in the trapping field mass  $m = 3.3 \times 10^{-13} m_{\text{Pl}}$  and  $g^2 = 0.81$ . The quartic self-coupling strength  $\lambda$  is chosen such that the vacuum energy vanishes, i.e.  $\lambda = 5/24 \cdot m^4/V(\phi_c) = 1.14 \times 10^{-24}$ .

The duration of inflation from the moment the pivot scale exits the horizon to the end of inflation is  $N = 41.5$  e-folds in this model. It is somewhat shorter than the conventional range from 50 to 60 e-folds. Nevertheless this value is sufficient to solve HBB problems, as detailed in section V. Indeed, the discussed model falls within the green region of Fig. 5.

The numerically computed spectrum is shown in the left panel of Fig. 6. In that plot we also provide the spectrum (the blue curve) computed using slow-roll approximation [48]

$$\mathcal{P}_\zeta(k) = \frac{1}{24\pi^2 m_{\text{Pl}}^4} \left. \frac{V}{\epsilon} \right|_k, \quad (60)$$

where  $\epsilon$  is defined in Eq. (10) and the index ‘ $k$ ’ indicates that  $\epsilon$  and  $V$  values must be evaluated at the horizon crossing. As one expects, this expression provides a good approximation of the spectrum for small  $k$ , but it starts deviating from the more accurate, numerically computed spectrum once the resonant production of  $\chi$  particles commences.

In the right panel of Fig. 6 we also show the spectrum of the isocurvature perturbation. As one can see, it is negligible on the CMB scales (small  $k$  values), which is required in order to satisfy the tight bounds on this mode from Planck constraints [51].

In addition to the Newton gauge expressions, we also perform the same simulations for perturbations in the flat gauge (see Appendix A), which provides a check of our computations. The results of the latter are not shown, because they are virtually indistinguishable from the Newtonian gauge ones.

## VII. MASS DISTRIBUTION OF PRIMORDIAL BLACK HOLES

In this section we calculate the mass function (i.e., the mass distribution) of PBHs as predicted by the current model. Roughly speaking we need the curvature perturbation to be of order  $\mathcal{P}_\zeta(k) \sim \mathcal{O}(10^{-1.5})$ , so that during radiation domination PBHs are produced via gravitational collapse. Then, the relation between the mass of PBHs and the wave number  $k$  can be written by

$$m_{\text{PBH}} \sim 10^{20} \text{g} \left( \frac{k_*}{10^{14} \text{Mpc}^{-1}} \right)^{-2}. \quad (61)$$

This corresponds to  $N \sim 35$  e-folds after the pivot scale exits the horizon.

Having the spectrum of the primordial curvature perturbation  $\mathcal{P}_\zeta$  (see Fig. 6) we can compute the abundance of PBHs following, for example, Ref. [22].

First, let us define the fraction of the energy density of PBHs relative to that of Cold Dark Matter (CDM) evaluated at present time

$$f_{\text{PBH}} \equiv \frac{\rho_{\text{PBH}}}{\rho_{\text{CDM}}}, \quad (62)$$

where  $\rho_{\text{PBH}}$  and  $\rho_{\text{CDM}}$  denote energy densities of PBHs and CDM respectively. Then the mass function per logarithmic bin in mass  $df_{\text{PBH}}(m_{\text{PBH}})/d\ln(m_{\text{PBH}}) \sim f_{\text{PBH}}(m_{\text{PBH}})$  can be expressed as

$$f_{\text{PBH}}(m_{\text{PBH}}) = \frac{\Omega_{\text{m}}}{\Omega_{\text{CDM}}} \left[ \frac{g_*(T)}{g_*(T_{\text{eq}})} \frac{g_{*,s}(T_{\text{eq}})}{g_{*,s}(T)} \frac{T(m_{\text{PBH}})}{T_{\text{eq}}} \gamma^\beta(m_{\text{PBH}}) \right], \quad (63)$$

where we used the fraction  $\beta$  of the energy density of PBHs  $\rho_{\text{PBH}}$  relative to the total energy density  $\rho_{\text{tot}}$  at the formation epoch,  $\beta \equiv \rho_{\text{PBH}}/\rho_{\text{tot}}$ . In the above expression,  $\Omega_{\text{m}}$  and  $\Omega_{\text{CDM}}$  denote cosmological density parameters of matter and CDM respectively. For these parameters we adopt the values reported by the Planck team in Ref. [51]. Also,  $g_*$ ,  $g_{*,s}$  denote the number of relativistic degrees of freedom that contribute to the energy and entropy densities respectively. We use their concrete time-dependent values as reported in Ref. [77]. Temperatures  $T(m_{\text{PBH}})$  and  $T_{\text{eq}}$  are evaluated at the formation of PBHs and at the matter-radiation equality respectively, while constant  $\gamma$  denotes the ratio between the mass of the PBHs  $m_{\text{PBH}}$  and the horizon mass  $M_{\text{H}} = \frac{4\pi}{3} \frac{\rho}{H^3}$  given by

$$m_{\text{PBH}} = \gamma M_{\text{H}}, \quad (64)$$

where the energy density  $\rho$  is computed using the Friedmann equation,  $\rho = 3m_{\text{Pl}}^2 H^2$ , and  $H$  is the Hubble parameter evaluated at the time of PBH formation. According to a simple analytic formula, the value of  $\gamma$  is estimated to be  $\gamma = (1/\sqrt{3})^3 \sim 0.2$  [78].

Assuming that the density perturbation follows Gaussian distribution, we can compute  $\beta$  using the Press Schechter theory [79], which gives

$$\beta(m_{\text{PBH}}) = \int_{\delta_c}^{\infty} \frac{d\delta}{\sqrt{2\pi}\sigma(m_{\text{PBH}})} \exp\left[\frac{-\delta^2}{2\sigma^2(m_{\text{PBH}})}\right] = \frac{1}{2} \text{Erfc}\left[\frac{\delta_c}{\sqrt{2}\sigma(m_{\text{PBH}})}\right]. \quad (65)$$

As it is clear from the above,  $\beta$  is a function of the PBH mass, similarly to Eq. (63). Here Erfc denotes the complementary error function. The threshold  $\delta_c$  represents the critical value for PBH formation. The analytical expression for this quantity was computed in Ref. [80]. In this work, we adopt the value  $\delta_c = 0.45$  [81]. The density perturbation that exceeds this threshold value undergoes gravitational collapse when it re-enters the Hubble horizon, leading to the formation of PBHs.

Furthermore, applying the asymptotic expansion of the complementary error function in Eq. (65), we obtain

$$\beta(\sigma) \simeq \frac{\sigma(m_{\text{PBH}})}{\sqrt{2\pi}\delta_c} \exp\left[\frac{-\delta_c^2}{2\sigma^2(m_{\text{PBH}})}\right], \quad (66)$$

where  $\sigma$  is the coarse-grained density perturbation given by

$$\sigma^2(k) = \int_{-\infty}^{\infty} d \ln q W^2\left(\frac{q}{k}\right) \frac{4(1+w_{\text{eos}})^2}{(5+3w_{\text{eos}})^2} \left(\frac{q}{k}\right)^4 \mathcal{P}_{\zeta}(q), \quad (67)$$

and  $w_{\text{eos}}$  denotes the equation of state parameter, which is defined by  $w_{\text{eos}} = p/\rho$ , while  $W$  denotes the window function, which is taken to be  $W(k) = \exp(-k^2/2)$ .

Putting all together, the PBH abundance reaches the value  $f_{\text{PBH}} \sim \mathcal{O}(1)$  in the current model. Moreover, the mass of the PBHs peaks at  $m_{\text{PBH}} \sim 10^{19.5}$  g which is within the asteroid-mass range ( $10^{17}$  g  $\lesssim m_{\text{PBH}} \lesssim 10^{23}$  g) where the observational upper limits (see the colored curves in Fig. 7) still allow for the possibility of PBHs being 100% of CDM.

## VIII. INDUCED GRAVITATIONAL WAVES

The large amplitude of the curvature perturbation  $\mathcal{P}_{\zeta}$  on small scales, which is responsible for the formation of PBHs, is also responsible for the (stochastic) induced gravitational waves (SIGWs) that are generated via nonlinear second-order effects. In this section, we calculate the spectrum of such GWs that are produced during the radiation-dominated epoch. For the computation we follow the method detailed in Refs. [37, 40, 95] and adapt it to the current model. The detailed calculation is presented in Appendix B, where the present day spectrum is found to be

$$\Omega_{\text{GW}}(\eta, k) = \frac{\rho_{\text{GW}}(\eta, k)}{\rho_{\text{tot}}(\eta)} = \frac{1}{24} \left( \frac{k}{a(\eta)H(\eta)} \right)^2 \overline{\mathcal{P}_T(\eta, k)}. \quad (68)$$

In this expression  $\eta$  denotes the conformal time, and the wave number  $k$  is related to the frequency  $f$  by  $k = 2\pi f$ . The quantity  $\rho_{\text{GW}}(\eta, k)$  denotes the energy density of GWs per logarithmic interval of the wave number, and the overline  $\overline{\mathcal{P}_T}$  indicates the oscillation average of the tensor perturbation power spectrum  $\mathcal{P}_T(\eta, k)$ . This quantity is defined as

$$\mathcal{P}_T(\eta, k) = 4 \int_0^{\infty} dv \int_{|1-v|}^{1+v} du \left( \frac{4v^2 - (1+v^2-u^2)^2}{4vu} \right)^2 I^2(v, u, x) \mathcal{P}_{\zeta}(kv) \mathcal{P}_{\zeta}(ku), \quad (69)$$

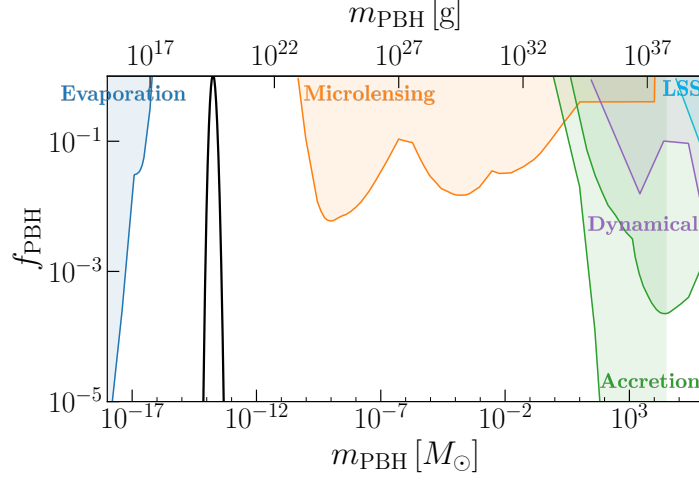


Figure 7. The mass distribution of PBHs (black curve) calculated by the spectrum given in Fig. 6 as a function of the PBH mass. The vertical axis indicates the energy fraction of PBHs to the CDM ( $f_{\text{PBH}}$ ). The colored curves represent observational upper bounds on  $f_{\text{PBH}}$  [23, 27]. The blue curve corresponds to constraints from the evaporation of the PBHs, including the extragalactic  $\gamma$ -ray background (EGB) [23, 27], the Voyager positron flux (V) [82], and annihilation-line radiation from the Galactic Centre (GC) [83]. The orange curve shows constraints from gravitational lensing, including those from supernovae (SN) [84], the M31 stars observed by Subaru/HSC [29], the Magellanic Clouds by EROS and MACHO (EM) [85, 86], and the Galactic bulge by the OGLE (O) [87]. The green curve shows the constraints from accretion, including X-ray binaries (XB) [88] and the spectral distortions of the CMB measured by Planck (PA) [89]. The purple curve represents the dynamical constraints, including those from wide binaries (WB) [90], star clusters in Eridanus II (E) [91], halo dynamical-friction (DF) [92], galaxy tidal-distortions (G) [93], heating of stars in the Galactic disk (DH) [92], and the CMB dipole (CMB). The cyan curve indicates constraints from large-scale structure formation [92, 94].

where  $x$  is the dimensionless variable  $x = k\eta$ , while  $u = |\mathbf{k} - \tilde{\mathbf{k}}|/k$  and  $v = \tilde{k}/k$  are integration variables representing the momentum configuration. The function  $I(v, u, x)$  is an oscillating function from the source information. From the expression for GWs, the spectrum includes the scalar perturbations through the source term of the tensor perturbation. The mean free path of weakly interacting light particles such as neutrinos damps the scalar field perturbations on small scales during the radiation-dominated epoch. Therefore, it also affects induced gravitational waves [39, 96, 97]. Next, we present the kernel function for the case with dissipative effect and discuss the expression of the kernel function without dissipation in Appendix B, which is shown by the black dashed curve in Fig. 8. The effect on the oscillating function  $I$  of the source term is given by

$$I_j^{(0)} = -\frac{1 - c_s^2(u^2 + v^2)}{2c_s^4 u^2 v^2} \left( 1 - \frac{1 - c_s^2(u^2 + v^2)}{4c_s^2 uv} [\text{cei}[(1 - c_s(u - v))] + \text{cei}[(1 + c_s(u - v))] \right. \\ \left. - \text{cei}[(1 - c_s(u + v))] - \text{cei}[(1 + c_s(u + v))] \right], \quad (70)$$

$$I_y^{(0)} = \frac{(1 - c_s^2(u^2 + v^2))^2}{8c_s^6 u^3 v^3} (\text{Sei}[(1 - c_s(u - v))] + \text{Sei}[(1 + c_s(u - v))] \\ - \text{Sei}[(1 - c_s(u + v))] - \text{Sei}[(1 + c_s(u + v))]), \quad (71)$$

where the subscript  $j$  and  $y$  denote that the oscillating function is divided into terms of the spherical Bessel function of order zero. Furthermore, the superscript (0) on  $I$  denotes the term separated by the order of differentiation of  $F = (k_D(\tau)/k_D(\tau_*))^{-2}$ , which is normalized by the damping scale  $k_D(\tau_*)$  at the pivot scale. The functions  $\text{cei}$  and  $\text{Sei}$  are given by

$$\text{cei}(y) = \int_0^\infty \frac{dx}{x} e^{-(u^2 + v^2)\kappa_D^2 F[x/x_*]} [1 - \cos(yx)], \quad (72)$$

$$\text{Sei}(y) = \int_0^\infty \frac{dx}{x} e^{-(u^2 + v^2)\kappa_D^2 F[x/x_*]} \sin(yx), \quad (73)$$

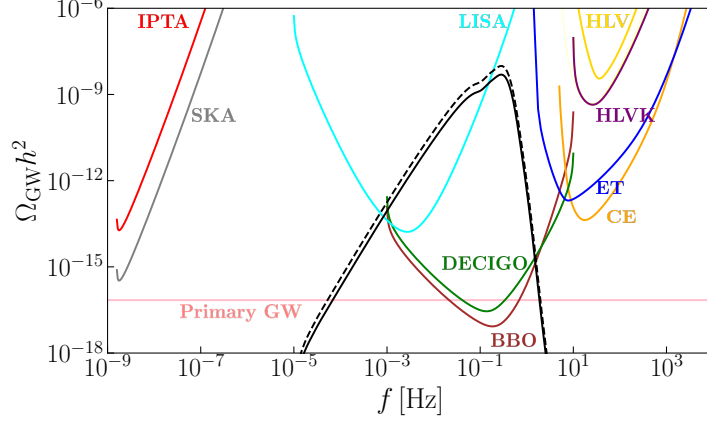


Figure 8. Energy density of gravitational waves  $\Omega_{\text{GW}} h^2$  as a function of the frequency  $f$  in units of Hz, where  $h$  is the dimensionless Hubble constant. The black dashed curve represents the spectrum of SIGWs, the black solid curve shows GWs with the dissipation, and the pink curve marks the approximate amplitude of primary GWs. Other colored curves show the sensitivities of various gravitational wave observatories [98]. They are the International Pulsar Timing Array (IPTA) (red) [99–102], the Square Kilometre Array (SKA) (grey) [103–105], the Laser Interferometer Space Antenna (LISA) (cyan) [106, 107], the Deci-Hertz Interferometer Gravitational-Wave Observatory (DECIGO) (green) [108–111], the Big-Bang Observer (BBO) (brown) [111–114], the Hanford-Livingston-Virgo (HLV) (yellow) [115–117], the Hanford-Livingston-Virgo-KAGRA (HLVK) (purple) [118, 119], the Einstein Telescope (ET) (blue) [120–123], and the Cosmic Explorer (CE) (orange) [124, 125].

where  $c_s^2 = 1/3$  is the sound speed, and  $\kappa_D = k/k_D(\tau_*)$  is the dimensionless  $k$  normalized by the damping scale at the pivot scale.

The result is shown in Fig. 8. The black solid curve in that figure represents the spectrum of the induced GWs that are generated by scalar perturbations at second order in perturbation theory and are computed above, while the dashed black curve is the same without dissipation effect. As pointed out in Ref. [39, 96, 97], this effect is also found to dissipate the peak and the low-frequency tail of GWs. The pink line shows an approximate spectrum of primary GWs that are generated by vacuum fluctuations during inflation. Other colored curves indicate sensitivity bounds of future planned GW observations (see the caption of Fig. 8 for details). The figure shows that it becomes evident that our model predicts GWs which fall within the detectability limits of LISA, DECIGO and BBO future observatories.

## IX. GRAVITATIONAL WAVES FROM MERGING BINARY PBHS

There is one more source of GWs. As binary PBHs merge they also induce a stochastic GW background [40–42]. We compute the spectrum of such GWs in this section.

Details of the calculation are provided in Appendix C, where it is shown that the spectrum obeys the following relation

$$\Omega_{\text{GW}}^{(\text{merger})}(f) = \frac{f}{\rho_c} \int_0^{z_{\text{sup}}} dz \frac{R(z)}{(1+z)H(z)} \frac{dE(f_s)}{df_s}. \quad (74)$$

In this expression  $\rho_c$  denotes the critical energy density of the Universe.  $z$  is the redshift and  $z_{\text{sup}}$  is the upper limit of integration, which is computed as  $z_{\text{sup}} = f_3/f - 1$ , where  $f_3$  is the cutoff frequency of GW at the end of the ringdown phase of BH merger [40].

$R(z)$  represents the PBH merger rate and  $dE(f_s)/df_s$  denotes the energy spectrum of the gravitational wave emitted from the source. Detailed expressions of these functions are provided in Appendix C.

As shown in Fig. 7, the abundance of PBHs in our model exhibits a pronounced peak at  $m_{\text{PBH}} \sim 3 \times 10^{19} \text{g}$  with  $f_{\text{PBH}} \sim \mathcal{O}(1)$ . The GW spectrum that is produced by mergers of such PBHs is shown in Fig. 9. As can be seen in the figure, GW spectrum falls within the sensitivity region of resonant cavity detectors [43, 44].

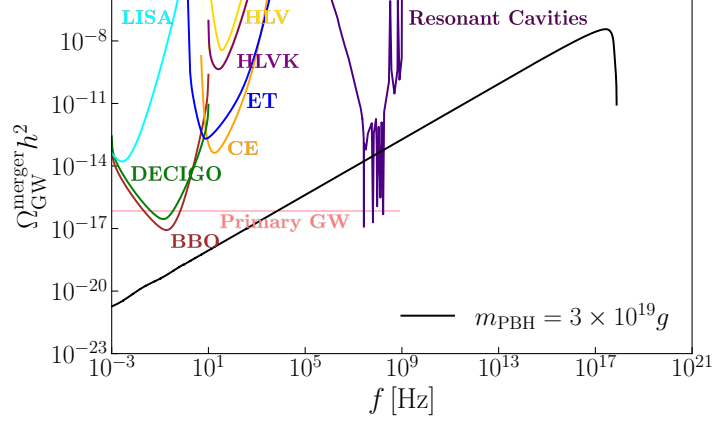


Figure 9. The spectrum of GWs generated by PBH mergers (black curve). Other coloured curves are the same as in Fig. 8 in addition to the resonant cavity experiment [43, 44] (dark purple curve).

## X. CONCLUSIONS AND DISCUSSION

In this work we study a multi-field inflation scenario with a tachyonic trap in the context of supersymmetric running-mass-inflation models. The scenario is reminiscent of hybrid inflation with some modifications. Initially the inflaton field rolls down the running-mass potential. When the critical point  $\phi_{\text{SBP}}$  is reached, which we called the symmetry breaking point, the waterfall field is resonantly excited. Such excitations backreact onto the motion of the inflaton field anchoring its value at  $\phi_{\text{SBP}}$ . The remaining number of e-folds of inflation are generated during the waterfall phase. To make this phase long enough, the potential in the waterfall direction must be sufficiently flat.

The proposed scenario enables us to model running-mass-inflation from the time when observable scales exit the horizon to the end of inflation. It also allows us to compute the spectrum of the curvature perturbation for the full duration of inflation. We find that the spectrum exhibits a sharp peak, corresponding to the scales which exit the horizon around SBP. The enhancement of the spectrum at these scales is due to the shape of the running-mass potential. Additionally the resonance amplifies the amplitude of the spectrum by several orders of magnitude more.

Such a large perturbation gives rise to PBHs with masses in the range  $10^{17} \text{ g} - 10^{23} \text{ g}$ , which are viable dark matter candidates. The same perturbation also sources induced gravitational waves in the deci-Hz range, providing a natural signal for upcoming space-based interferometers such as LISA, DECIGO, and BBO. Furthermore, PBHs formed in this scenario can subsequently assemble into binaries, whose mergers generate gravitational waves observable both in resonant cavity experiments via the inverse Gertsenshtein effect and in future space-based detectors. Although we have not explicitly addressed the effects of stochastic noise on the motion of the inflaton in this work, for the parameter ranges considered, we estimate such effects to remain subdominant, which justifies neglecting them.

## ACKNOWLEDGMENTS

This work was in part supported by JSPS KAKENHI Grants Nos. JP23KF0289, JP24K07027 (K.K.), MEXT KAKENHI Grants No. JP24H01825 (K.K.), and by the Spanish Research Agency (Agencia Estatal de Investigación) through national project CNS2022-13600, AEI/MCIU through grant PID2023-148162NB-C21 and ASFAE/2022/020 (A.S.).

## Appendix A: The Primordial Perturbation in the Flat Gauge

In the flat gauge the scalar part of the spatial curvature perturbation vanishes. This allows us to write the perturbed line element as

$$ds^2 = -(1 + 2\alpha) dt^2 - 2a\beta_{,i} dx^i dt + a^2 (\delta_{ij} + 2\partial_i \partial_j \gamma) dx^i dx^j, \quad (\text{A1})$$



where  $\alpha$  is the perturbation of the lapse,  $\beta$  is the scalar part of the perturbation of the shift and  $\gamma$  is a scalar function. In this gauge the equations for the field perturbation can be written as [48]

$$\delta\ddot{\varphi}_{kI} + 3H\delta\dot{\varphi}_{kI} + \frac{k^2}{a^2}\delta\varphi_{kI} + V_{,IJ}\delta\varphi_k^J = a^{-3}\frac{d}{dt}\left(\frac{a^3}{H}\dot{\varphi}_I\dot{\varphi}_J\right)\delta\varphi_k^J, \quad (\text{A2})$$

where repeated indices imply summation and for brevity we used the notation  $\varphi_I = (\phi, \chi)$  and similarly for the perturbation. The potential  $V(\phi, \chi)$  is provided in Eq. (43). For the homogeneous value of the  $\chi$  field, we used the same expression as in Eq. (39).

Due to spatial homogeneity of the background FRW metric perturbation variables  $\beta$  and  $\gamma$  come in the combination given by [126]<sup>1</sup>

$$\Psi_k \equiv a(\beta_k + a\dot{\gamma}_k). \quad (\text{A3})$$

This variable satisfies the equation

$$2H\frac{k^2}{a^2}\Psi_k = -\dot{\varphi}_I\delta\dot{\varphi}^I + \left(\ddot{\varphi}_I + \frac{\dot{\varphi}_J\dot{\varphi}^J}{2H}\dot{\varphi}_I\right)\delta\varphi_k^I. \quad (\text{A4})$$

In terms of these variables the curvature perturbation on the uniform density slice  $\zeta$  is given by

$$\zeta_k = -\frac{H\left(\dot{\varphi}_I\delta\varphi_k^I + \frac{2}{3}\frac{k^2}{a^2}\Psi_k\right)}{\dot{\varphi}_I\dot{\varphi}^I}. \quad (\text{A5})$$

In order to check our numerical computations we run the simulations in the Newtonian and flat gauges independently and then check if they give consistent results. To perform the comparison we need the expressions that relate the various quantities in the two gauges. The final result for  $\zeta$  can be checked by comparing Eq. (A5) above with Eq. (50). But we also compare intermediate quantities. For example, the Newtonian curvature perturbation  $\Phi_k$  in Eq. (36) and  $\Psi_k$  in Eq. (A3) above are related by

$$\Phi_k = H\Psi_k. \quad (\text{A6})$$

We checked numerically that  $\Phi_k$  computed solving Newtonian gauge equations coincide exactly with the flat gauge solution of  $\Psi_k$  after performing the conversion of the latter to  $\Phi_k$  using the above equation. Similarly, we can compare the scalar field perturbations.

Similar conclusions hold for the field perturbations too. Such perturbations in the two gauges are related by

$$\delta\varphi_k^I|_{\text{Newt}} = \delta\varphi_k^I|_{\text{flat}} - \dot{\varphi}^I\Psi_k. \quad (\text{A7})$$

Again, the LHS of this equation, as computed from Eqs. (44) and (45), coincides with the RHS, as computed using Eqs. (A2) and (A4).

## Appendix B: Detailed computations of induced gravitational waves

In this section, we introduce the detailed computations of the spectrum of induced gravitational waves in the radiation-dominated epoch [36, 37, 95], which were only summarized in Section VIII. Here we do not consider non-gaussian perturbation for simplicity [127–129]. As given in Eq. (68), the spectrum of induced gravitational waves is expressed to be

$$\Omega_{\text{GW}}(\eta, k) = \frac{\rho_{\text{GW}}(\eta, k)}{\rho_{\text{tot}}(\eta)} = \frac{1}{24} \left( \frac{k}{a(\eta)H(\eta)} \right)^2 \overline{\mathcal{P}_T(\eta, k)}, \quad (\text{B1})$$

where  $\eta$  is the conformal time, the wave number  $k$  is related to the GW frequency  $f$  via  $k = 2\pi f$ , and  $\rho_{\text{GW}}(\eta, k)$  is the energy density of gravitational waves per logarithmic wave number. The overline denotes the oscillation average.  $\mathcal{P}_T(\eta, k)$  is the power spectrum of the tensor perturbation  $T$  which is expressed by

$$\mathcal{P}_T(\eta, k) = 4 \int_0^\infty dv \int_{|1-v|}^{1+v} du \left( \frac{4v^2 - (1+v^2-u^2)^2}{4vu} \right)^2 I^2(v, u, x) \mathcal{P}_\zeta(kv) \mathcal{P}_\zeta(ku), \quad (\text{B2})$$

---

<sup>1</sup> The  $\Psi$  symbol here should not be confused with the metric perturbation in the Newtonian gauge in Eq. (36).

where  $x$  is the dimensionless variable  $x = k\eta$ . The variables  $u$  and  $v$  are defined by  $u = |\mathbf{k} - \tilde{\mathbf{k}}|/k$  and  $v = \tilde{k}/k$ , respectively. The function  $I(v, u, x)$  is an oscillating kernel function encoding the source information given by

$$I(v, u, x) = \int_0^x d\bar{x} \frac{a(\bar{\eta})}{a(\eta)} k G_k(\eta, \bar{\eta}) f(v, u, \bar{x}), \quad (\text{B3})$$

where  $G_k$  is the Green's function, defined by the solution to the differential equation

$$G_k''(\eta, \bar{\eta}) + (k^2 - a''(\eta)/a(\eta)) G_k(\eta, \bar{\eta}) = \delta(\eta - \bar{\eta}), \quad (\text{B4})$$

with primes denoting derivatives with respect to  $\eta$ . The function  $f(v, u, \bar{x})$  represents the source term constructed from second-order scalar perturbations. Since the kernel function  $I$  with dissipation has been presented in Sec. VIII, this Appendix provides the expression for the kernel function without dissipative effect, which is shown by the black dashed curve in Fig. 8. To evaluate the spectrum of GWs observed at present, we take the late-time limit  $\eta \rightarrow \infty$ , or equivalently  $x \gg 1$ . In addition, if we take the oscillation average in this limit, we obtain

$$\begin{aligned} \overline{I_{\text{RD}}^2(v, u, x \rightarrow \infty)} &= \frac{1}{2} \left( \frac{3(u^2 + v^2 - 3)}{4u^3v^3x} \right)^2 \left( \left( -4uv + (u^2 + v^2 - 3) \log \left| \frac{3 - (u+v)^2}{3 - (u-v)^2} \right| \right)^2 \right. \\ &\quad \left. + \pi^2(u^2 + v^2 - 3)^2 \Theta(v + u - \sqrt{3}) \right), \end{aligned} \quad (\text{B5})$$

where  $\Theta$  denotes the Heaviside theta function. Furthermore, as pointed out in Ref. [37], due to the symmetry under the exchange of  $u$  and  $v$ , we can perform a change of variables from  $(u, v)$  to  $(t, s)$  with  $t = u + v - 1$  and  $s = u - v$ . Under this transformation, the oscillation-averaged kernel function becomes

$$\begin{aligned} \overline{I_{\text{RD}}^2(t, s, x \rightarrow \infty)} &= \frac{288(-5 + s^2 + t(2+t))^2}{x^2(1-s+t)^6(1+s+t)^6} \left( \frac{\pi^2}{4} (-5 + s^2 + t(2+t))^2 \Theta(t - (\sqrt{3} - 1)) \right. \\ &\quad \left. + \left( -(t-s+1)(t+s+1) + \frac{1}{2}(-5 + s^2 + t(2+t)) \log \left| \frac{-2+t(2+t)}{3-s^2} \right| \right)^2 \right). \end{aligned} \quad (\text{B6})$$

Rewriting the power spectrum of the tensor perturbations  $\mathcal{P}_T(\eta, k)$  in terms of the new variables  $s$  and  $t$ , one obtains

$$\mathcal{P}_T(\eta, k) = 2 \int_0^\infty dt \int_{-1}^1 ds \left[ \frac{t(2+t)(s^2-1)}{(1-s+t)(1+s+t)} \right]^2 I^2(t, s, x \rightarrow \infty) \mathcal{P}_\zeta \left( k \frac{t-s+1}{2} \right) \mathcal{P}_\zeta \left( k \frac{t+s+1}{2} \right). \quad (\text{B7})$$

### Appendix C: Detailed computations of gravitational waves from merging binary PBHs

In this section, we discuss the details of the computations of the gravitational wave spectrum emitted from merging binary PBHs [40–42] which was only summarized in Section IX. The spectrum of gravitational waves from the PBH mergers is given by Eq. (74), which we write here again

$$\Omega_{\text{GW}}^{(\text{merger})}(f) = \frac{f}{\rho_c} \int_0^{z_{\text{sup}}} dz \frac{R(z)}{(1+z)H(z)} \frac{dE(f_s)}{df_s}, \quad (\text{C1})$$

where the Hubble parameter is given by  $H(z) = H_0[\Omega_r(1+z)^4 + \Omega_m(1+z)^3 + \Omega_\Lambda]^{1/2}$  with  $\Omega_r$  and  $\Omega_\Lambda = 1 - \Omega_r - \Omega_m$  being the  $\Omega$  parameters of radiation, and the present-day cosmological constant, respectively. The quantity  $R(z)$  denotes the rate of the mergers for the binary PBHs per comoving volume for a PBH mass  $m_{\text{PBH}}$ , given by

$$R(z) = \frac{f_{\text{PBH}} \Omega_{\text{CDM}} \rho_c}{m_{\text{PBH}}} \frac{dP_t}{dt}, \quad (\text{C2})$$

where  $dP_t/dt$  is the probability distribution for a PBH merger occurring at time  $t$ , given by

$$\frac{dP_t}{dt} = \frac{3}{58t} \times \begin{cases} \left( \frac{t}{T_{\text{per}}} \right)^{3/37} - \left( \frac{t}{T_{\text{per}}} \right)^{3/8} & (t < t_c) \\ \left( \frac{t}{T_{\text{per}}} \right)^{3/8} \left( \left( \frac{t}{t_c} \right)^{-29/56} \left( \frac{4\pi f_{\text{PBH}}}{3} \right)^{-29/8} - 1 \right) & (t \geq t_c) \end{cases}, \quad (\text{C3})$$

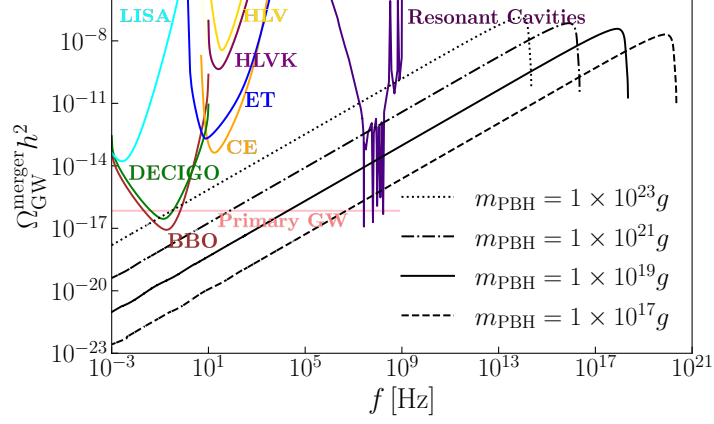


Figure 10. GW spectrum generated by PBH mergers. The horizontal axis represents the frequency  $f$  in units of Hz, while the vertical axis corresponds to the energy density of the gravitational waves originating from PBH mergers, denoted by  $\Omega_{\text{GW}}^{\text{merger}} h^2$ , where  $h$  is the dimensionless Hubble parameter. The black curve represents the spectrum of the gravitational waves from mergers of PBH with  $10^{17}\text{g}$  (dashed),  $10^{19}\text{g}$  (solid),  $10^{21}\text{g}$  (dot-dashed), and  $10^{23}\text{g}$  (dashed) respectively within the sensitivity range of resonant cavities of axion. Furthermore, the signal from PBHs with  $10^{23}\text{g}$  (dotted line) can be observed within the sensitivity of reach not only the resonant cavities of axion but also DECIGO and BBO. The pink curve approximately corresponds to the spectrum of primary gravitational waves. The other colored curves indicate the sensitivity curves of future planned gravitational-wave observatories [98], and resonant cavities for the axion detection [43, 44].

with  $t_c$  defined by  $t_c = (4\pi f_{\text{PBH}}/3)^{37/3} T_{\text{per}}$  and  $T_{\text{per}}$  given by

$$T_{\text{per}} = \frac{729}{340\pi^2(1+z_{\text{eq}})^4(4\pi f_{\text{PBH}}^{16} m_{\text{PBH}}^5 \rho_c^4/3)^{1/3}}, \quad (\text{C4})$$

where  $z_{\text{eq}}$  is the redshift at the epoch of matter-radiation equality. The typical time  $t$  at which mergers occur is given by

$$t = \int_z^\infty \frac{dz'}{(1+z')H(z')}, \quad (\text{C5})$$

In Eq. (74), the GW energy spectrum of a non-spinning PBH binary from the source,  $dE(f_s)/df_s$ , is modeled as

$$\frac{dE(f_s)}{df_s} = \frac{(G\pi)^{2/3} M_c^{5/3}}{3} \begin{cases} f_s^{-1/3} & \text{for } f_s < f_1; \text{ inspiral phase} \\ w_1 f_s^{2/3} & \text{for } f_1 \leq f_s < f_2; \text{ merger phase} \\ w_2 \frac{f_s^2}{(1 + \frac{4(f_s - f_2)^2}{\sigma^2})^2} & \text{for } f_2 \leq f_s \leq f_3; \text{ ringdown phase} \\ 0, & \text{for } f_3 < f_s \end{cases} \quad (\text{C6})$$

where  $f_s = (1+z)f$  denotes the frequency emitted at the source,  $G$  is the Newton's gravitational constant and  $M_c$  is the chirp mass defined by  $M_c^{5/3} = m_{\text{PBH},1} m_{\text{PBH},2} / (m_{\text{PBH},1} + m_{\text{PBH},2})^{1/3}$ . The parameters  $w_1$  and  $w_2$  are fitting coefficients chosen to ensure the continuity of the spectrum, given by  $w_1 = f_1^{-1}$  and  $w_2 = f_1^{-1} f_2^{-4/3}$ .  $f_1$ ,  $f_2$ ,  $f_3$ , and  $\sigma$  are given

$$\pi M_t f_1 = (1 - 4.455 + 3.521) + 0.6437\eta - 0.05822\eta^2 - 7.092\eta^3 \quad (\text{C7})$$

$$\pi M_t f_2 = (1 - 0.63)/2 + 0.1469\eta - 0.0249\eta^2 + 2.325\eta^3 \quad (\text{C8})$$

$$\pi M_t f_3 = 0.3236 - 0.1331\eta - 0.2714\eta^2 + 4.922\eta^3 \quad (\text{C9})$$

$$\pi M_t \sigma = (1 - 0.63)/4 - 0.4098\eta + 1.829\eta^2 - 2.87\eta^3, \quad (\text{C10})$$

where the total mass  $M_t = m_{\text{PBH},1} + m_{\text{PBH},2}$  and the symmetric mass ratio  $\eta = m_{\text{PBH},1} m_{\text{PBH},2} / (m_{\text{PBH},1} + m_{\text{PBH},2})^2$ .

We now consider the asteroid-mass range ( $10^{17}\text{g} \lesssim m_{\text{PBH}} \lesssim 10^{23}\text{g}$ ), in which an abundance  $f_{\text{PBH}} \sim \mathcal{O}(1)$  is allowed under observational constraints to become the 100% CDM. Within this mass range, we choose four benchmark values,

$10^{17}g$ ,  $10^{19}g$ ,  $10^{21}g$ , and  $10^{23}g$ , and compute the corresponding spectra of the gravitational waves from the PBH mergers. These plots are shown as the black curves in Fig. 10.

- 
- [1] L. Kofman, A. D. Linde, X. Liu, A. Maloney, L. McAllister, and E. Silverstein, JHEP **05**, 030, arXiv:hep-th/0403001 [hep-th].
  - [2] D. Green, B. Horn, L. Senatore, and E. Silverstein, Phys. Rev. D **80**, 063533 (2009), arXiv:0902.1006 [hep-th].
  - [3] D. J. Chung, E. W. Kolb, A. Riotto, and I. I. Tkachev, Phys. Rev. D **62**, 043508 (2000), arXiv:hep-ph/9910437 [hep-ph].
  - [4] O. Elgaroy, S. Hannestad, and T. Haugboelle, JCAP **09**, 008, arXiv:astro-ph/0306229.
  - [5] A. E. Romano and M. Sasaki, Phys. Rev. D **78**, 103522 (2008), arXiv:0809.5142 [gr-qc].
  - [6] N. Barnaby, Z. Huang, L. Kofman, and D. Pogosyan, Phys. Rev. D **80**, 043501 (2009), arXiv:0902.0615 [hep-th].
  - [7] N. Barnaby, Adv. Astron. **2010**, 156180 (2010), arXiv:1010.5507 [astro-ph.CO].
  - [8] L. Pearce, M. Peloso, and L. Sorbo, JCAP **05**, 054, arXiv:1702.07661 [astro-ph.CO].
  - [9] Y.-F. Cai, J. Jiang, M. Sasaki, V. Vardanyan, and Z. Zhou, Phys. Rev. Lett. **127**, 251301 (2021), arXiv:2105.12554 [astro-ph.CO].
  - [10] J. F. Dufaux, G. N. Felder, L. Kofman, M. Peloso, and D. Podolsky, JCAP **0607**, 006, arXiv:hep-ph/0602144 [hep-ph].
  - [11] K. Dimopoulos, M. Karčiauskas, and C. Owen, Phys. Rev. D **100**, 083530 (2019), arXiv:1907.04676 [hep-ph].
  - [12] M. Karčiauskas, S. Rusak, and A. Saez, Phys. Rev. D **105**, 043535 (2022), arXiv:2112.11536 [astro-ph.CO].
  - [13] S. M. Leach, I. J. Grivell, and A. R. Liddle, Phys. Rev. D **62**, 043516 (2000), arXiv:astro-ph/0004296 [astro-ph].
  - [14] A. D. Linde, Phys. Rev. D **49**, 748 (1994).
  - [15] E. J. Copeland, A. R. Liddle, D. H. Lyth, E. D. Stewart, and D. Wands, Phys. Rev. D **49**, 6410 (1994), arXiv:astro-ph/9401011.
  - [16] K. Kohri, D. H. Lyth, and A. Melchiorri, JCAP **04**, 038, arXiv:0711.5006 [hep-ph].
  - [17] L. Alabidi and K. Kohri, Phys. Rev. D **80**, 063511 (2009), arXiv:0906.1398 [astro-ph.CO].
  - [18] L. Alabidi, K. Kohri, M. Sasaki, and Y. Sendouda, JCAP **09**, 017, arXiv:1203.4663 [astro-ph.CO].
  - [19] L. Alabidi, K. Kohri, M. Sasaki, and Y. Sendouda, JCAP **05**, 033, arXiv:1303.4519 [astro-ph.CO].
  - [20] K. Inomata, M. Kawasaki, K. Mukaida, Y. Tada, and T. T. Yanagida, Phys. Rev. D **96**, 043504 (2017), arXiv:1701.02544 [astro-ph.CO].
  - [21] K. Inomata, M. Kawasaki, K. Mukaida, Y. Tada, and T. T. Yanagida, Phys. Rev. D **95**, 123510 (2017), arXiv:1611.06130 [astro-ph.CO].
  - [22] K. Kohri and T. Terada, Class. Quant. Grav. **35**, 235017 (2018), arXiv:1802.06785 [astro-ph.CO].
  - [23] B. Carr, K. Kohri, Y. Sendouda, and J. Yokoyama, Rept. Prog. Phys. **84**, 116902 (2021), arXiv:2002.12778 [astro-ph.CO].
  - [24] B. Carr and F. Kuhnel, Ann. Rev. Nucl. Part. Sci. **70**, 355 (2020), arXiv:2006.02838 [astro-ph.CO].
  - [25] A. M. Green and B. J. Kavanagh, J. Phys. G **48**, 043001 (2021), arXiv:2007.10722 [astro-ph.CO].
  - [26] A. Escrivà, F. Kuhnel, and Y. Tada, 10.1016/B978-0-32-395636-9.00012-8 (2022), arXiv:2211.05767 [astro-ph.CO].
  - [27] B. Carr, K. Kohri, Y. Sendouda, and J. Yokoyama, Phys. Rev. D **81**, 104019 (2010), arXiv:0912.5297 [astro-ph.CO].
  - [28] H. Niihara *et al.*, Nature Astron. **3**, 524 (2019), arXiv:1701.02151 [astro-ph.CO].
  - [29] N. Smyth, S. Profumo, S. English, T. Jeltema, K. McKinnon, and P. Guhathakurta, Phys. Rev. D **101**, 063005 (2020), arXiv:1910.01285 [astro-ph.CO].
  - [30] S. Mollerach, D. Harari, and S. Matarrese, Phys. Rev. D **69**, 063002 (2004), arXiv:astro-ph/0310711.
  - [31] K. N. Ananda, C. Clarkson, and D. Wands, Phys. Rev. D **75**, 123518 (2007), arXiv:gr-qc/0612013.
  - [32] D. Baumann, P. J. Steinhardt, K. Takahashi, and K. Ichiki, Phys. Rev. D **76**, 084019 (2007), arXiv:hep-th/0703290.
  - [33] R. Saito and J. Yokoyama, Phys. Rev. Lett. **102**, 161101 (2009), [Erratum: Phys. Rev. Lett. **107**, 069901 (2011)], arXiv:0812.4339 [astro-ph].
  - [34] E. Bugaev and P. Klimai, Phys. Rev. D **81**, 023517 (2010), arXiv:0908.0664 [astro-ph.CO].
  - [35] H. Assadullahi and D. Wands, Phys. Rev. D **79**, 083511 (2009), arXiv:0901.0989 [astro-ph.CO].
  - [36] J. R. Espinosa, D. Racco, and A. Riotto, JCAP **09**, 012, arXiv:1804.07732 [hep-ph].
  - [37] K. Kohri and T. Terada, Phys. Rev. D **97**, 123532 (2018), arXiv:1804.08577 [gr-qc].
  - [38] R.-G. Cai, S. Pi, and M. Sasaki, Phys. Rev. D **102**, 083528 (2020), arXiv:1909.13728 [astro-ph.CO].
  - [39] G. Domènech and J. Chluba, JCAP **07**, 034, arXiv:2503.13670 [gr-qc].
  - [40] M. Sasaki, T. Suyama, T. Tanaka, and S. Yokoyama, Class. Quant. Grav. **35**, 063001 (2018), arXiv:1801.05235 [astro-ph.CO].
  - [41] S. Wang, T. Terada, and K. Kohri, Phys. Rev. D **99**, 103531 (2019), [Erratum: Phys. Rev. D **101**, 069901 (2020)], arXiv:1903.05924 [astro-ph.CO].
  - [42] K. Kohri, T. Terada, and T. T. Yanagida, Phys. Rev. D **111**, 063543 (2025), arXiv:2409.06365 [astro-ph.CO].
  - [43] A. Berlin, D. Blas, R. Tito D'Agnolo, S. A. R. Ellis, R. Harnik, Y. Kahn, and J. Schütte-Engel, Phys. Rev. D **105**, 116011 (2022), arXiv:2112.11465 [hep-ph].
  - [44] N. Herman, L. Lehoucq, and A. Füzfa, Phys. Rev. D **108**, 124009 (2023), arXiv:2203.15668 [gr-qc].
  - [45] E. D. Stewart, Phys. Lett. B **391**, 34 (1997), arXiv:hep-ph/9606241 [hep-ph].
  - [46] E. D. Stewart, Phys. Rev. D **56**, 1919 (1997), arXiv:hep-ph/9703232.
  - [47] L. Covi, D. H. Lyth, and L. Roszkowski, Phys. Rev. D **60**, 023509 (1999), arXiv:hep-ph/9809310 [hep-ph].

- [48] D. Lyth and A. Liddle, *The Primordial Density Perturbation: Cosmology, Inflation and the Origin of Structure* (Cambridge University Press, 2009).
- [49] S. Kachru, R. Kallosh, A. D. Linde, J. M. Maldacena, L. P. McAllister, and S. P. Trivedi, JCAP **0310**, 013, arXiv:hep-th/0308055 [hep-th].
- [50] S. Iso, K. Kohri, and K. Shimada, Phys. Rev. D **91**, 044006 (2015), arXiv:1408.2339 [hep-ph].
- [51] Y. Akrami *et al.* (Planck), Astron. Astrophys. **641**, A10 (2020), arXiv:1807.06211 [astro-ph.CO].
- [52] W. H. Kinney, Phys. Rev. D **56**, 2002 (1997), arXiv:hep-ph/9702427.
- [53] S. Inoue and J. Yokoyama, Phys. Lett. B **524**, 15 (2002), arXiv:hep-ph/0104083.
- [54] W. H. Kinney, Phys. Rev. D **72**, 023515 (2005), arXiv:gr-qc/0503017.
- [55] J. Martin, H. Motohashi, and T. Suyama, Phys. Rev. D **87**, 023514 (2013), arXiv:1211.0083 [astro-ph.CO].
- [56] P. A. R. Ade *et al.* (Planck), Astron. Astrophys. **571**, A22 (2014), arXiv:1303.5082 [astro-ph.CO].
- [57] T. Louis *et al.* (ACT), (2025), arXiv:2503.14452 [astro-ph.CO].
- [58] E. Calabrese *et al.* (ACT), (2025), arXiv:2503.14454 [astro-ph.CO].
- [59] P. A. R. Ade *et al.* (BICEP, Keck), Phys. Rev. Lett. **127**, 151301 (2021), arXiv:2110.00483 [astro-ph.CO].
- [60] T. Bringmann, P. Scott, and Y. Akrami, Phys. Rev. D **85**, 125027 (2012), arXiv:1110.2484 [astro-ph.CO].
- [61] K. Inomata and T. Nakama, Phys. Rev. D **99**, 043511 (2019), arXiv:1812.00674 [astro-ph.CO].
- [62] L. Kofman, A. Linde, and A. A. Starobinsky, Phys. Rev. D **56**, 3258 (1997), arXiv:hep-ph/9704452 [hep-ph].
- [63] G. N. Felder, L. Kofman, and A. D. Linde, Phys. Rev. D **64**, 123517 (2001), arXiv:hep-th/0106179 [hep-th].
- [64] D. Battefeld, T. Battefeld, C. Byrnes, and D. Langlois, JCAP **08**, 025, arXiv:1106.1891 [astro-ph.CO].
- [65] S. S. Naik, K. Furuuchi, and P. Chingangbam, JCAP **07** (07), 016, arXiv:2202.05862 [astro-ph.CO].
- [66] H. Kodama and T. Hamazaki, Prog. Theor. Phys. **96**, 949 (1996), arXiv:gr-qc/9608022.
- [67] B. A. Bassett, F. Tamburini, D. I. Kaiser, and R. Maartens, Nucl. Phys. B **561**, 188 (1999), arXiv:hep-ph/9901319.
- [68] J. T. Giblin and A. J. Tishue, Phys. Rev. D **100**, 063543 (2019), arXiv:1907.10601 [gr-qc].
- [69] B. Eggemeier, P. Hayman, J. C. Niemeyer, and R. Easther, Phys. Rev. D **109**, 043521 (2024), arXiv:2311.08780 [astro-ph.CO].
- [70] C. Gordon, D. Wands, B. A. Bassett, and R. Maartens, Phys. Rev. D **63**, 023506 (2001), arXiv:astro-ph/0009131 [astro-ph].
- [71] T. Murata and Y. Tada, (2025), arXiv:2507.22439 [astro-ph.CO].
- [72] J. Martin and V. Vennin, Phys. Rev. D **85**, 043525 (2012), arXiv:1110.2070 [astro-ph.CO].
- [73] M. Kawasaki, K. Kohri, and N. Sugiyama, Phys. Rev. Lett. **82**, 4168 (1999), arXiv:astro-ph/9811437.
- [74] S. Hannestad, Phys. Rev. D **70**, 043506 (2004), arXiv:astro-ph/0403291 [astro-ph].
- [75] P. F. de Salas, M. Lattanzi, G. Mangano, G. Miele, S. Pastor, and O. Pisanti, Phys. Rev. D **92**, 123534 (2015), arXiv:1511.00672 [astro-ph.CO].
- [76] J.-O. Gong and M. Mylova, (2022), arXiv:2202.13882 [hep-th].
- [77] K. Saikawa and S. Shirai, JCAP **08**, 011, arXiv:2005.03544 [hep-ph].
- [78] B. J. Carr, Astrophys. J. **201**, 1 (1975).
- [79] W. H. Press and P. Schechter, Astrophys. J. **187**, 425 (1974).
- [80] T. Harada, C.-M. Yoo, and K. Kohri, Phys. Rev. D **88**, 084051 (2013), [Erratum: Phys. Rev. D **89**, no.2, 029903 (2014)], arXiv:1309.4201 [astro-ph.CO].
- [81] I. Musco, J. C. Miller, and L. Rezzolla, Class. Quant. Grav. **22**, 1405 (2005), arXiv:gr-qc/0412063.
- [82] M. Boudaud and M. Cirelli, Phys. Rev. Lett. **122**, 041104 (2019), arXiv:1807.03075 [astro-ph.HE].
- [83] B. J. Carr, K. Kohri, Y. Sendouda, and J. Yokoyama, Phys. Rev. D **94**, 044029 (2016), arXiv:1604.05349 [astro-ph.CO].
- [84] P. W. Graham, S. Rajendran, and J. Varela, Phys. Rev. D **92**, 063007 (2015), arXiv:1505.04444 [hep-ph].
- [85] P. Tisserand *et al.* (EROS-2), Astron. Astrophys. **469**, 387 (2007), arXiv:astro-ph/0607207.
- [86] R. A. Allsman *et al.* (Macho), Astrophys. J. Lett. **550**, L169 (2001), arXiv:astro-ph/0011506.
- [87] H. Niikura, M. Takada, S. Yokoyama, T. Sumi, and S. Masaki, Phys. Rev. D **99**, 083503 (2019), arXiv:1901.07120 [astro-ph.CO].
- [88] Y. Inoue and A. Kusenko, JCAP **10**, 034, arXiv:1705.00791 [astro-ph.CO].
- [89] H. Tashiro and N. Sugiyama, Phys. Rev. D **78**, 023004 (2008), arXiv:0801.3172 [astro-ph].
- [90] M. A. Monroy-Rodríguez and C. Allen, The Astrophysical Journal **790**, 159 (2014).
- [91] S. L. Zoutendijk, J. Brinchmann, L. A. Boogaard, M. L. P. Gunawardhana, T.-O. Husser, S. Kamann, A. F. Ramos Padilla, M. M. Roth, R. Bacon, M. den Brok, S. Dreizler, and D. Krajnović, Astronomy, Astrophysics **635**, A107 (2020).
- [92] B. Carr and J. Silk, Mon. Not. Roy. Astron. Soc. **478**, 3756 (2018), arXiv:1801.00672 [astro-ph.CO].
- [93] B. J. Carr and M. Sakellariadou, Astrophys. J. **516**, 195 (1999).
- [94] R. Murgia, G. Scelfo, M. Viel, and A. Raccanelli, Phys. Rev. Lett. **123**, 071102 (2019), arXiv:1903.10509 [astro-ph.CO].
- [95] T. Terada, (2025), arXiv:2509.18694 [gr-qc].
- [96] D. Jeong, J. Pradler, J. Chluba, and M. Kamionkowski, Phys. Rev. Lett. **113**, 061301 (2014), arXiv:1403.3697 [astro-ph.CO].
- [97] Y.-H. Yu, Z. Chang, and S. Wang (2025) arXiv:2510.18663 [gr-qc].
- [98] K. Schmitz, JHEP **01**, 097, arXiv:2002.04615 [hep-ph].
- [99] G. Hobbs, A. Archibald, Z. Arzoumanian, D. Backer, M. Bailes, N. D. R. Bhat, M. Burgay, S. Burke-Spolaor, D. Champion, I. Cognard, W. Coles, J. Cordes, P. Demorest, G. Desvignes, R. D. Ferdman, L. Finn, P. Freire, M. Gonzalez, J. Hessels, A. Hotan, G. Janssen, F. Jenet, A. Jessner, C. Jordan, V. Kaspi, M. Kramer, V. Kondratiev, J. Lazio, K. Lazaridis, K. J. Lee, Y. Levin, A. Lommen, D. Lorimer, R. Lynch, A. Lyne, R. Manchester, M. McLaughlin, D. Nice, S. Osłowski, M. Pilia, A. Possenti, M. Purver, S. Ransom, J. Reynolds, S. Sanidas, J. Sarkissian, A. Sesana, R. Shannon,

- X. Siemens, I. Stairs, B. Stappers, D. Stinebring, G. Theureau, R. van Haasteren, W. van Straten, J. P. W. Verbiest, D. R. B. Yardley, and X. P. You, *Classical and Quantum Gravity* **27**, 084013 (2010).
- [100] R. N. Manchester, *Classical and Quantum Gravity* **30**, 224010 (2013).
- [101] J. P. W. Verbiest, L. Lentati, G. Hobbs, R. van Haasteren, P. B. Demorest, G. H. Janssen, J.-B. Wang, G. Desvignes, R. N. Caballero, M. J. Keith, D. J. Champion, Z. Arzoumanian, S. Babak, C. G. Bassa, N. D. R. Bhat, A. Brazier, P. Brem, M. Burgay, S. Burke-Spolaor, S. J. Chamberlin, S. Chatterjee, B. Christy, I. Cognard, J. M. Cordes, S. Dai, T. Dolch, J. A. Ellis, R. D. Ferdman, E. Fonseca, J. R. Gair, N. E. Garver-Daniels, P. Gentile, M. E. Gonzalez, E. Graikou, L. Guillemot, J. W. T. Hessels, G. Jones, R. Karuppusamy, M. Kerr, M. Kramer, M. T. Lam, P. D. Lasky, A. Lassus, P. Lazarus, T. J. W. Lazio, K. J. Lee, L. Levin, K. Liu, R. S. Lynch, A. G. Lyne, J. Mckee, M. A. McLaughlin, S. T. McWilliams, D. R. Madison, R. N. Manchester, C. M. F. Mingarelli, D. J. Nice, S. Osłowski, N. T. Palliyaguru, T. T. Pennucci, B. B. P. Perera, D. Perrodin, A. Possenti, A. Petiteau, S. M. Ransom, D. Reardon, P. A. Rosado, S. A. Sanidas, A. Sesana, G. Shaifullah, R. M. Shannon, X. Siemens, J. Simon, R. Smits, R. Spiewak, I. H. Stairs, B. W. Stappers, D. R. Stinebring, K. Stovall, J. K. Swiggum, S. R. Taylor, G. Theureau, C. Tiburzi, L. Toomey, M. Vallisneri, W. van Straten, A. Vecchio, Y. Wang, L. Wen, X. P. You, W. W. Zhu, and X.-J. Zhu, *Monthly Notices of the Royal Astronomical Society* **458**, 1267 (2016).
- [102] J. S. Hazboun, C. M. F. Mingarelli, and K. Lee, (2018), arXiv:1810.10527 [astro-ph.IM].
- [103] C. L. Carilli and S. Rawlings, *New Astron. Rev.* **48**, 979 (2004), arXiv:astro-ph/0409274.
- [104] G. Janssen *et al.*, PoS **AASKA14**, 037 (2015), arXiv:1501.00127 [astro-ph.IM].
- [105] A. Weltman *et al.*, *Publ. Astron. Soc. Austral.* **37**, e002 (2020), arXiv:1810.02680 [astro-ph.CO].
- [106] P. Amaro-Seoane, H. Audley, S. Babak, J. Baker, E. Barausse, P. Bender, E. Berti, P. Binetruy, M. Born, D. Bortoluzzi, J. Camp, C. Caprini, V. Cardoso, M. Colpi, J. Conklin, N. Cornish, C. Cutler, K. Danzmann, R. Dolesi, L. Ferraioli, V. Ferroni, E. Fitzsimons, J. Gair, L. G. Bote, D. Giardini, F. Gibert, C. Grimaldi, H. Halloin, G. Heinzel, T. Hertog, M. Hewitson, K. Holley-Bockelmann, D. Hollington, M. Hueller, H. Inchauspe, P. Jetzer, N. Karnesis, C. Killow, A. Klein, B. Klipstein, N. Korsakova, S. L. Larson, J. Livas, I. Lloro, N. Man, D. Mance, J. Martino, I. Mateos, K. McKenzie, S. T. McWilliams, C. Miller, G. Mueller, G. Nardini, G. Nelemans, M. Nofrarias, A. Petiteau, P. Pivato, E. Plagnol, E. Porter, J. Reiche, D. Robertson, N. Robertson, E. Rossi, G. Russano, B. Schutz, A. Sesana, D. Shoemaker, J. Slutsky, C. F. Sopuerta, T. Sumner, N. Tamanini, I. Thorpe, M. Troebs, M. Vallisneri, A. Vecchio, D. Vetrugno, S. Vitale, M. Volonteri, G. Wanner, H. Ward, P. Wass, W. Weber, J. Ziemer, and P. Zweifel, *Laser interferometer space antenna* (2017), arXiv:1702.00786 [astro-ph.IM].
- [107] J. Baker *et al.*, (2019), arXiv:1907.06482 [astro-ph.IM].
- [108] N. Seto, S. Kawamura, and T. Nakamura, *Phys. Rev. Lett.* **87**, 221103 (2001), arXiv:astro-ph/0108011 [astro-ph].
- [109] S. Kawamura *et al.*, *Class. Quant. Grav.* **23**, S125 (2006).
- [110] K. Yagi and N. Seto, *Phys. Rev. D* **83**, 044011 (2011), [Erratum: *Phys.Rev.D* 95, 109901 (2017)], arXiv:1101.3940 [astro-ph.CO].
- [111] S. Isoyama, H. Nakano, and T. Nakamura, *PTEP* **2018**, 073E01 (2018), arXiv:1802.06977 [gr-qc].
- [112] J. Crowder and N. J. Cornish, *Phys. Rev. D* **72**, 083005 (2005), arXiv:gr-qc/0506015.
- [113] V. Corbin and N. J. Cornish, *Class. Quant. Grav.* **23**, 2435 (2006), arXiv:gr-qc/0512039.
- [114] G. M. Harry, P. Fritschel, D. A. Shaddock, W. Folkner, and E. S. Phinney, *Class. Quant. Grav.* **23**, 4887 (2006), [Erratum: *Class.Quant.Grav.* 23, 7361 (2006)].
- [115] J. Kissel (LIGO Scientific, Virgo), *H1 Calibrated Sensitivity Spectra Jun 10 2017 (Representative Best of O2 - C02, With Cleaning / Subtraction)*. (), <https://dcc.ligo.org/LIGO-G1801950/public>.
- [116] J. Kissel (LIGO Scientific, Virgo), *L1 Calibrated Sensitivity Spectra Aug 06 2017 (Representative Best of O2 - C02, With Cleaning / Subtraction)*. (), <https://dcc.ligo.org/LIGO-G1801952/public>.
- [117] *GWTC-1: Fig. 1 .*, <https://dcc.ligo.org/LIGO-P1800374/public>.
- [118] L. Barsotti, P. Fritschel, M. Evans, and S. Gras (LIGO Scientific, Virgo), *Updated Advanced LIGO sensitivity design curve*, <https://dcc.ligo.org/LIGO-T1800044/public>.
- [119] C. Berry, S. Fairhurst, B. O'Reilly, M. Razzano, and P. J. Sutton (LIGO Scientific, Virgo), *Prospects for Observing and Localizing Gravitational-Wave Transients with Advanced LIGO, Advanced Virgo and KAGRA*, <https://dcc.ligo.org/LIGO-P1200087-v47/public>.
- [120] M. Punturo *et al.*, *Proceedings, 14th Workshop on Gravitational wave data analysis (GWDAA-14): Rome, Italy, January 26-29, 2010*, *Class. Quant. Grav.* **27**, 194002 (2010).
- [121] S. Hild *et al.*, *Class. Quant. Grav.* **28**, 094013 (2011), arXiv:1012.0908 [gr-qc].
- [122] B. Sathyaprakash *et al.*, *Class. Quant. Grav.* **29**, 124013 (2012), [Erratum: *Class.Quant.Grav.* 30, 079501 (2013)], arXiv:1206.0331 [gr-qc].
- [123] M. Maggiore *et al.* (ET), *JCAP* **03**, 050, arXiv:1912.02622 [astro-ph.CO].
- [124] B. P. Abbott *et al.* (LIGO Scientific), *Class. Quant. Grav.* **34**, 044001 (2017), arXiv:1607.08697 [astro-ph.IM].
- [125] D. Reitze *et al.*, *Bull. Am. Astron. Soc.* **51**, 035 (2019), arXiv:1907.04833 [astro-ph.IM].
- [126] J.-c. Hwang, *Astrophys.J.* **375**, 443 (1991).
- [127] R.-g. Cai, S. Pi, and M. Sasaki, *Phys. Rev. Lett.* **122**, 201101 (2019), arXiv:1810.11000 [astro-ph.CO].
- [128] J.-P. Li, S. Wang, Z.-C. Zhao, and K. Kohri, *JCAP* **06**, 039, arXiv:2309.07792 [astro-ph.CO].
- [129] J.-P. Li, S. Wang, Z.-C. Zhao, and K. Kohri, *JCAP* **05**, 109, arXiv:2403.00238 [astro-ph.CO].